Structurally Folded Curvature Surface Models of Geodes/Agate Rosettes (Cathode/Anode) as Vehicle/Truck Storage for High Energy Density Lithium-Ion Batteries

Hesham Khalifa,[a, c] Sherif A. El-Safty,*[a] Abdullah Reda,[a] Mohamed A. Shenashen,[a] Ahmed Elmarakbi,[b] and Hussain A. Metawa[c]

The synchronized development of low cost, high energy density, full-scale lithium-ion battery (LIB) vehicle/truck storages with long charge/discharge cycles, long-term stability, and excellent rate capacity and Coulombic efficiency is crucial. Here, structurally folded curvature surface cathode/anode models were designated as vehicle/truck storages. The modulation of LIB vehicle folds with diverse surface functions such as cave-in-hollow nests, shell-walled/fenced edges, and convex/concave spheroid-capped gradients of geode (G)/agate rosette (AR) (cathode/anode) electrodes may be used as leverage to motivate the dynamic mobility of electron-ion motion systems directly and generate vehicle/truck storage loading on sustainable electrode surface geometrics, leading to long-term charge/discharge cycles. In this vehicle/truck storage design, evidence of the effect of structurally folded curvature surface models on the creation of anode/cathode designs is first reported as the force-driven modulation of high energy density of full-scale G-cathode//AR-anode LIBs. The built-in LIB is formulated with structurally shaped spheroids along whole-, eroded-, and unopened G-cathodes and AR-anodes that exhibit the effect of the remarkable surface curvature function changes on fabrication of well-defined geometric LIBs. The building design of G-cathode//AR-anode LIBs with a bundle of convex/concave spheroid-capped gradients, and three-dimensional (3D) surface curvatures offer a massive gate-in transport of electrons/Li^+ ions for long periods of charge/discharge cycles and outstanding discharge capacities. Outstanding long-term cycling performance and stability, excellent retention capacity $\sim 85\%$ with a first discharge specific capacity of 162.5 mAh g^{-1} and an approximate Coulombic efficiency of 99.7%, were obtained after 2000 cycles at a rate of 1 C in a potential region from 0.8 V to 3.5 V versus Li/Li$^+$ at room temperature by using 3D super-scalable G@C//AR@C built-in full-scale LIB models. A high value of specific energy density ≈ 131.6 Wh kg^{-1}. The full-scale LIB models may offer all mandatory requirements overcoming the energy density limits that required a driving range of long-term EVs.

1. Introduction

A well-developed design for rechargeable lithium-ion batteries (LIBs) is crucial in the manufacture of environmentally clean and sustainable energy systems and power sources. Although cost-effective production routes of LIBs are remains challenges, considerable efforts have been dedicated to improving performance of rechargeable LIBs due to their high energy density, excellent rates, and long life cycles.[1,2] Modern electronic devices, such as laptops, electronic gadgets, camcorder cameras, and smartphones, have a wide range of LIB applications.[3] Therefore, developments of high energy density

and scalable LIBs have become essential in the last decade.[1] However, force-driven modulations of LIBs in the 21st-century applications still have many constraints due to their expensive capital cost and hazard problems.[1,2]

To date, the development of low cost LIB design with long-term durability and safe pack modulation in the field of green energy to meet the requirement of future renewable energy storage systems is of a particular interest. A scalable, safe LIB can widely expand its utilization in smart grids and portable electronic devices, and in next-generation zero emission transportation applications, such as plug-in hybrid and fully electric vehicles (EVs).[4,5] The international car market has reported difficulties in the development of LIBs due to cost-to-range proportions. The introduction of large-scale LIB applications has become an urgent demand. Therefore, considerable efforts in all aspects of LIB manufacture, including electrode synthesis, material fabrication, electrolytes, and assembly in full-scale design, are devoted to the fabrication of novel sustainable hybrid electrode materials with outstanding electrochemical properties.[6]

To involve lithium materials as positive cathode electrodes into the next generation of Li-ion secondary battery cathodes, hybrid LiMPO$_4$/olivine isostructures (where M is a transition metal; i.e., Mn, Fe, Co, or Ni) were firstly used for fabrication of

[a] H. Khalifa, Prof. S. A. El-Safty, A. Reda, Dr. M. A. Shenashen
National Institute for Materials Science (NIMS),
Sengen 1-2-1, Tsukuba, Ibaraki 305-0047, Japan
E-mail: sherif.elsafty@nims.go.jp
Homepage: https://samurai.nims.go.jp/profiles/sherif_elsafty

[b] Prof. A. Elmarakbi
Department of Mechanical & Construction Engineering, Faculty of Engineering and Environment,
Northumbria University, Newcastle upon Tyne, NE1 8ST, UK

[c] H. Khalifa, Prof. H. A. Metawa
Department of Physics, Faculty of Science,
Damanhur University, Damanhur, Egypt

Supporting information for this article is available on the WWW under https://doi.org/10.1002/batt.201900083

LIBs.[5,7] In particular, the polyanionic LiFePO$_4$ (LFPO), which exhibits a regular olivine structure, has attracted considerable attention from researchers recently.[4] The primary structural features, such as high capacity and long durability, of the LFPO architectural tectonics have made highly functional rechargeable Li batteries. The built-in LFPO tectonic in the cathode electrode design is a promising due to its high charge-discharge rate capability. LFPO is a better cathode material alternative than conventional ones, such as LiCoO$_2$, LiNiO$_2$, and LiMnO$_2$, due to its decreased toxicity and relatively low cost.[7] Moreover, theoretical studies on LFPO predicted enlarged capacity of up to 170 mAh g^{-1} and good cycling stability with good cyclic voltammetric behavior referred to as the two-phase extraction/insertion mechanism.[5,8] Thermal stability is another advantage of this material-based electrode that provides good safety pattern when the temperature increases, thereby resolving common problems such as overcharging and electrolyte decomposition. However, LFPO cathodes have poor electronic and ionic conductivity; low rate capability; sluggish electrode kinetics, Li$^+$ ion transport, and diffusion at the LiFePO$_4$/FePO$_4$ interface; and low tap density.[5,8,9] Several strategies, such as decreasing the particle size,[7,10] using highly conductive carbon coatings,[11,12] inserting conductive additives,[13] doping with supervalent metal ions,[13,14] and modifying the morphology by synthesizing 3D hierarchically structured materials with multi-diffusive open sites with desired crystal orientations,[14] have been used to effectively improve LFPO electrochemical performance. Various methods, such as hydrothermal process, sol-gel process, solvothermal treatment, co-precipitation, solid-state reaction, and emulsion drying, have obtained highly crystalline LFPO composites.[15–17] Among these, the hydrothermal method offers the most flexible and excellent way of synthesizing pure LFPO particles without impurities, superb efficiency, facile controlled size, and rapid reaction rate. LFPO materials with different morphologies may be controlled by using hydrothermal synthesis and changing the precursor type, thereby enhancing their electrochemical performance.[18] In this regard, the 3D hierarchical LFPO geometry used with micro-, meso-, and macro-diffusible structures, intraformational shell-rounded fence rims, and ridge-gate windows, and multi-exposed surface sites is critical to boost the facile electron/ion transportation with high load reversible capacity and excellent rate capability.[19] To date, if 3D hierarchical cathode electrodes can be fabricated in well-defined geometric vehicle/truck storage loading by using open-mouth cave-in-hollow-like nests, shell-walled/fenced edge-like sinks, and convex/concave spheroid-capped gradients for 3D surface curvature geodes,[20] then powerful built-in energy storage systems can be configured for scalable and commercial requirements of EV applications with respect to energy density, power, safety characteristics, and life cycle.

Owing to its abundance, low production cost, and reasonable theoretical capacity (372 mAh g^{-1}, LiC$_6$), graphite was used as an active anode Sony material in the first market generation of LIB.[21,22] However, severe structure collapse and exfoliation of graphite-anode material over cycling that generated from the formation of solid electrolyte interface (SEI) loads drastically accelerated the capacity rate etiolation. The low operating voltage of ~0.1 V vs. Li/Li$^+$ effectively enabled lithium electroplating at the graphite-anode electrode surface, which represents another problem due to safety issues.[23] At a high charging/discharging current rate, lithium dendrites can easily be formed on the graphite surface due to its high polarization.[22] Such dendrites can move through the separator resulting in an internal short circuit, cell damaging, and warming up until fire (thermal runaway),[24] leading to constrain graphite-anode electrode feasibility and fidelity to meet EVs requirements. Low cost and nontoxic anode electrodes in LIBs with effective surface function of electron/ion diffusion and multiple charge/discharge cycles are crucial in the extensive manufacturing of green energy.[25] Among all materials, TiO$_2$ (TO) structures are being pioneered as negative electrodes capable to overcome the disadvantages of graphite due to their enormous structural stability. Although the TO anode shows a relatively low reversible capacity compared to other transition oxides, but it exhibits superior cycling stability and Coulombic efficiency. TO offers an attractive surface and electrically effective site for fast kinetics Li$^+$ inflow.[24] The TO anode is suitable for LIB marketing due to its merits to solve of safety issues. However, the formation of lithium dendrites on TO-anode surfaces is effectively suppressed due to the higher delithiation potential (1.7 V vs. Li/Li+), making TO a safe anode material for various applications. Other functionalities of TO associated with its abundant, low cost, nontoxic and pollution-free nature, eco-friendliness, low polarization, high stability, and cycling reversibility make TO-anode a promising built-in LIB module.[25,26] The mobility in chemical composition gradients of the TO anode and the phase transition from tetragonal TiO$_2$ (space group I4$_1$/amd) into orthorhombic lithium-rich Li$_{0.5}$TiO$_2$ (space group Imma) may create lithium-rich surface sites along the central crystal and upper zones of the top surface of the atomic-scale arrangement of Li$_{0.5}$TiO$_2$ orthorhombic crystals.[27,28] The TO structure transition may also undergo a spontaneous conversion of lithium-poor Li$_{0.01}$TiO$_2$ phase into lithium-rich Li$_{0.5}$TiO$_2$, leading to the generation of a wide range of dynamic mobility surfaces. However, challenges remain in understanding the key roles of structural orientation, function surface curvatures, heterogeneity, and anisotropic composite formation of TO-anode electrodes in the formulation of well-defined geometric half- or full-cell LIBs.[19]

In this study, we report scalable and structurally folded heterogeneous curvature surface models of LFPO geodes (G@C-cathode)//TO agate rosettes (AR@C-anode) that differentially regulate structural vehicle folds as the force-driven modulation of high energy density of LIB-EVs. The built-in LFPO@C//AR@C LIB used with 3D-reconstructed curvature surface variations in cave-in-hollow nests; shell-walled/fenced edges; and structurally shaped spheroids along whole, eroded, and unopened geode dominants (WG-, EG-, and UG-cathodes) and agate rosettes (AR-anodes) exhibits remarkable surface curvature function changes in well-defined geometric LIBs. These 3D surface curvature vehicle folds create a bundle of convex/concave spheroid-capped gradients, a massive way-in transport of electron/ion for long periods, and outstanding

discharge capacities of built-in full-scale G@C//AR@C LIBs. Among all built-in LIB designs, the WG@C half-cell cathode-LIB design showed a significant increase in electrochemical performance with (i) capacity of 169.6 and 137.4 mAhg^{-1} at 0.1 and 20 C rates, respectively; (ii) durability of up to 2000 charge/discharge cycles without clear retro-gradation; and (iii) high energy density due to its relatively high tap density. The primary indicator of a promising candidate for next-generation high-power LIBs is the successful design of 3D super scalable G@C//AR@C built-in full-scale LIB models. The integration of the built-in full-scale LIB model with the WG@C (cathode)//AR@C (anode) generated long-term cycling performance (stability) with excellent discharge capacity retention (approximately 85%), average Coulombic efficiency of 99.7% after 2000 cycles at the 1 C discharge rate and voltage range of 0.8–3.5 V at room temperature. The dominant surface curvature folds is the force-driven modulation of full-scale WG-cathode//AR-anode LIBs similar to those of vehicle/truck storages with specific energy density of 131.6 Whkg^{-1}, which it is a substantial demand for the critical energy storage requirement. Overall, the built-in full-scale LIB meets the industrial and commercial demands of the EV driving range in terms of excellent specific capacities, high energy density, safety characteristics, and cycling durability.

2. Results and Discussion

2.1. Control Engineering of Geode Dominants (G@C-Cathode) and Agate Rosette (AR@C-Anode)

The built-in LIB formulated with structurally shaped spheroids with 3D-reconstructed curvature surface variations along whole, eroded, and unopened geode dominants (WG@C-, EG@C-, and UG@C-cathodes) and TO agate rosette (AR@C-anode) exhibits remarkable vehicle/truck storage loading in well-defined geometric LIBs. In these geometrically-oriented LIBs, the anisotropic heterogeneity of composites are formed by embedding the well-ordered and sustainable (approximately 5 nm) C-shell dressers along AR-anode/G-cathode structures. Structurally folded curvature surface models designated with cave-in-hollow nests, shell-walled/fenced edges, degree of 3D surface curvature, and convex/concave spheroid-capped gradients of geodes (G)/agate rosettes (AR) (cathode/anode) electrodes may be used as leverage to motivate the dynamic mobility of electron-ion motion systems directly, create vehicle/truck storage loading during long-term charge/discharge stability, and synchronize the development of full-scale LIB design with high energy density (Scheme 1).[29,30]
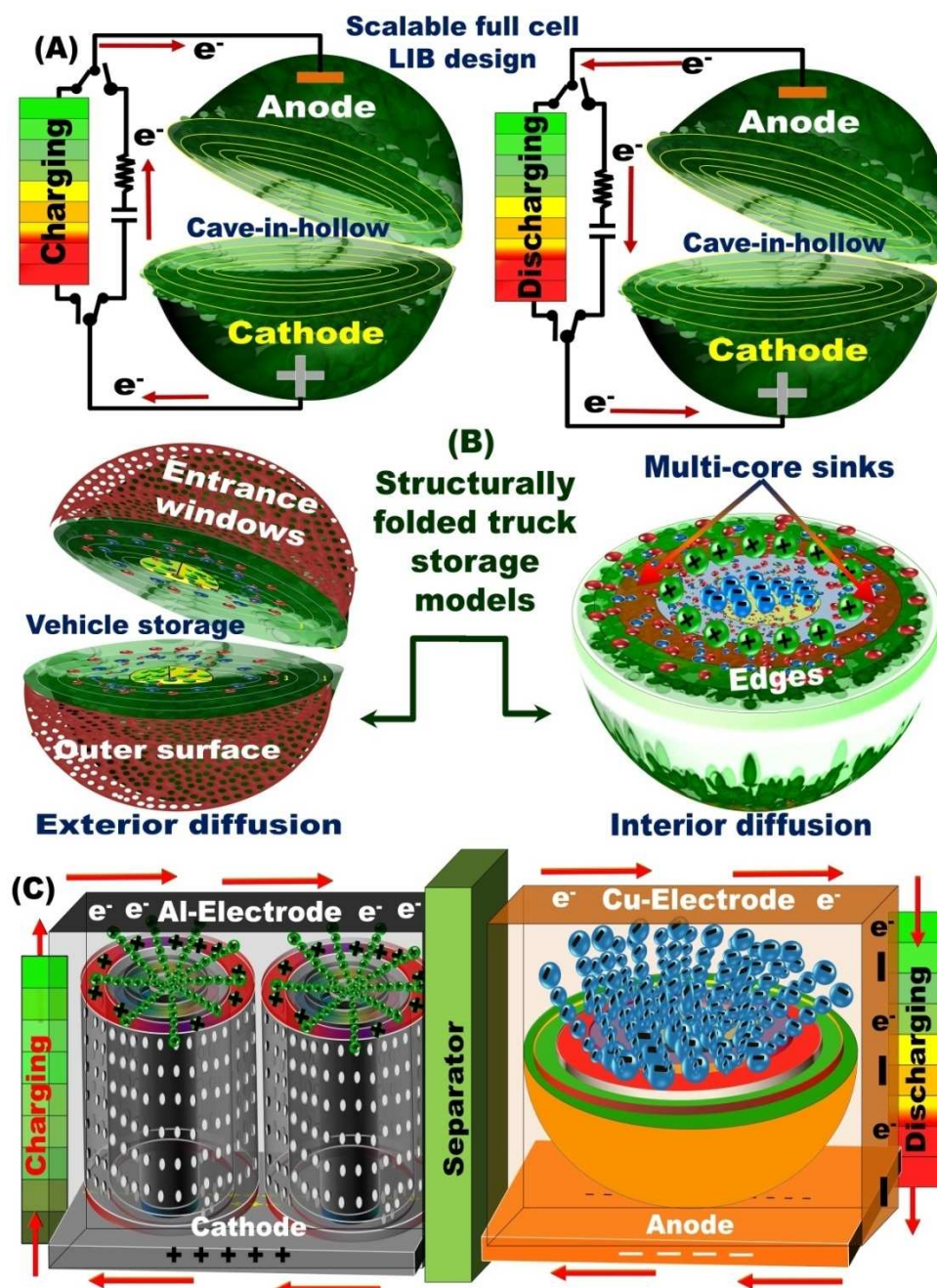
Therefore, a synthesis protocol is introduced to control the design of positive cathode electrode through manufacture of 3D hierarchically spheroid LFPO@C geode materials in nanoscale geometric objects used as G@C-cathodes, such as WG@C, EG@C, and UG@C geode spheroids, in LIBs. The 3D geometric G@C-cathode variables were tailored by adding variable lithium anions, such as chloride, fluoride, and nitrate, to the synthesis composition domains. In such anion-assisted geode syntheses,

the slipping from a relatively high-reducing agent precursor lithium nitrate toward a low-reducing lithium fluoride and chloride is crucial in changing the 3D structure spheroid-shaped model from the unopened geode (UG) structure passing through the eroded geode (EG) structure to the low-reducing power of the whole open geode (WG) structure. The low reducing power of Li-anion (i.e., chloride) can likely provide thermodynamic and kinetic time for well-developed building and seed growth of geodes with cave-in-hollow nests and shell-walled/fenced edges observed in WG-spheroid shapes. The Li anion (i.e., nitrate) with high reducing potential may sequentially boost the reaction kinetics and seed nucleation growth of geodes, thus leading to the formation of full-shell-walled spherule or UG structures.

To further understand the building growth of LFPO geode crystals (G-cathode) with various 3D-reconstructed curvature surface variations, our proposed synthesis protocol offers a sensible and force-driven modulation in controlling the dominant spheroid surface curvature as follows:

1) Typical structurally rich control variables, such as the (i) utilization of nucleation-directing agent and reagents and (ii) insertion rate of aqueous ethylene glycol and ethanol, can partially control the nucleation of the spherule-rich interstitial geode topography with Fe^{3+}/Fe^{2+} active espoused framework surfaces.

2) The control over time-dependent seed growth and high-temperature treatment of LFPO composite domains leads to thermodynamically formulated heterogeneous variable geode-spheroid G-structures.

3) The anion-assisted growth of LFPO with significant morphological modulations of structurally shaped spheroids with 3D-reconstructed curvature surface variations along whole, eroded, and unopened geode dominants could be due to the nucleation growth of geode dominants; the degree of convex/concave spheroid-capped gradients; and the dominant surface curvature kinetics, which are strongly force-driven by the strength of the Li precursor-reducing power.

The structurally shaped spheroids designated with 3D-reconstructed curvature surface variations along whole, eroded, and unopened geode dominants (G@C-cathode) and agate rosette (AR@C-anode) were investigated by using a variety of tools, including field emission scanning electron microscope (FE-SEM) and high-resolution transmission electron microscopy (HR-TEM) images (Figures 1 and 2 and Supporting information (SI) Figures S2 and S3). For example, Figures 1A (a, b, c, and d) and 1D (a, b, and c) depict low- and high-magnification images of FE-SEM and HR-TEM of the 3D hierarchical nanoscale geometric objects, respectively. The FE-SEM and HR-TEM micrographs show the formation of cave-in-hollow nests, spherule-rich interstitial core cavity-like sinks, and spheroid-shaped topography of G-cathodes. The WG@C morphology of 3D surface curvature geodes clearly demonstrated shell-walled/fenced edges and convex/concave spheroid-capped gradients. Among all structurally shaped spheroids, the WG@C geometric geode object is the most spherule-rich interstitial core cavity-like sinks with wide curvature surface folds. The primary characteristics of WG@C-cathode tectonics enabled to create

Scheme 1. (A) Scalable full cell LIB design in structurally-folded curvature surface models designated with cave-in-hollow, shell-walled/fenced edges, and convex/concave spheroid-capped gradients of 3D-surface curvature geodes (G)/agate rosettes (AR) (cathode/anode) electrodes. (B) The massive gate-in-transport and diffusional pathways of electron/Li$^+$ ion along open cave-in-hollow, spherule-rich interstitial core cavity-like sink, circularly-shaped topography, and 3D mesocages and open-mouth designated with G/AR (cathode/anode) electrodes. (C) Representative design of long term lithiation/delithiation (discharge/charge) cycling process using multiple layer-on-layer in 18650 cylindrical coil models for electric vehicles (LIB-EVs). (A–C) The full cell AR@C (anode)//G@C (LFPO@C) (cathode) electrodes with 3D reconstructed curvature surface variations oriented with structurally-shaped spheroids.

intensively multi-diffusible dimensions, open pore systems of connective meso-/macro-windows, inter-trapped cave spaces as nests, intraformational shell-rounded fence rims and ridge-gate windows, and multi-exposed crystal spherule surface sites. Although the structural uniqueness of WG@C-cathode is the force-driven modulation for excellent electrochemical performance and vehicle/truck storages, but other 3D G@C-cathode structures with EG@C, and UG@C geodes obtained, to relatively

high extent, multiple directional gates and high tap density, decreased the electron transport distance, and boosted the number of multi-diffusible ions in the electrodes and a wide range of transport pathways of Li$^+$ ions.

The result of the energy dispersive X-ray (EDX) spectroscopy shows the elemental mapping of the WG@C particle with percentage ratios of 61.4:19.1:17.9:1.6 for O:Fe:P:C elements (Figure 1B). Figures 1C-a, 1 C-b, S2, and S3 illustrate the high-
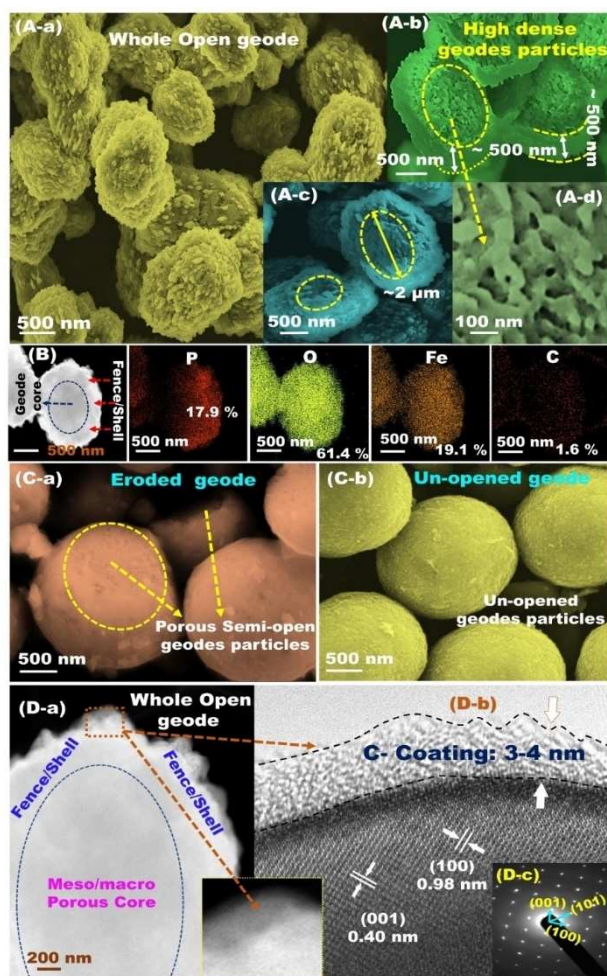
Figure 1. (A–D) FE-SEM, EDX-elemental mapping analysis, HR-TEM, and electron diffraction profiles of structurally-folded curvature surface models designated with cave-in-hollow, shell-walled/fenced edges, and convex/concave spheroid-capped gradients of 3D-surface curvature geodes (G-cathode) with whole open (WG@C), eroded (EG@C) and unopened (UG@C) spherules. (A-a) to (A-c) Low-magnification FE-SEM and (A-d) high magnifications FE-SEM of heterogeneous structurally-shaped whole-open geode spheroids (WG@C). (B) Energy-dispersive X-ray spectroscopy (EDX) and elemental mapping analysis (mass ratios) of WG@C geodes of O (61.4%), Fe (19.1%), P (17.9%), C (1.6%), respectively. Figure (C-a) and (C-b) represented the high magnification FE-SEM images of EG@C and UG@C, respectively. Figure (D-a) and (inset) showed low and high magnification HR-TEM micrographs of WG@C. Figure (D-b) High magnification HR-TEM of polyhedron lattice pattern at edge with clear thin layer 3–4 nm of C-coating on surface of WG crystals. Figure (D-c) Selected area electron diffraction (SAED) pattern of WG@C surface unit spherule with incident beam along the [010] crystallographic direction.

magnification images of heterogeneous eroded (EG@C) and unopened (UG@C) geode spheroid particles. Figures S2-D and S3-d show the elemental mapping of EG@C and UG@C spheroids with the percentage ratios of 61.6:17.9:18.6:1.9 and 64.1:16.7:17.3:1.9 for O:Fe:P:C elements, respectively.

Figures 1D(a–c), SI Figures S1D(a–c) and S2(e–g) show that the 3D WG@C, EG@C, and UG@C curvature surface architectures were further analyzed by using HR-TEM, respectively. The HR-TEM image recorded at the top-view edge of the spherule-rich WG@C cathode displays clear single-crystal planes with interatomic spacing of 0.4 and 0.98 nm, which refer to the (001)
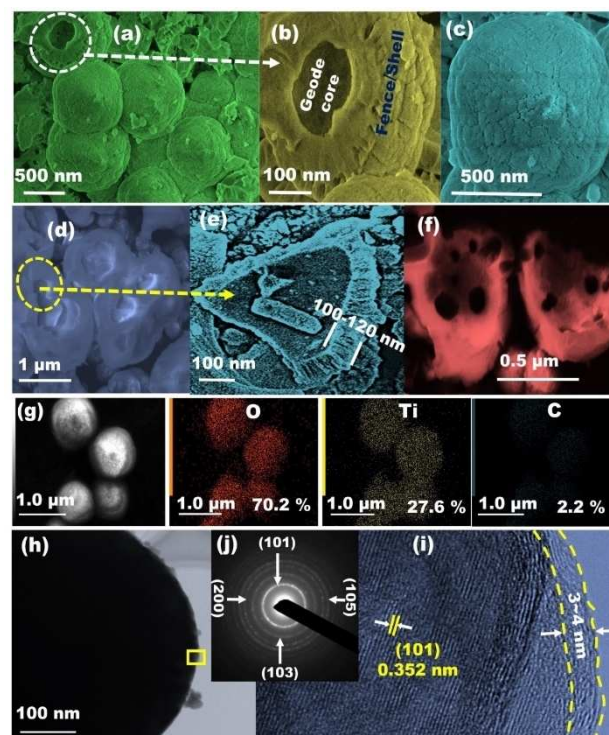

Figure 2. (a) and (b-f) Low and high magnification FE-SEM with top-concave and back-convex view of spheroid-capped gradients of 3D-surface curvature agate rosettes (AR) of anatase TO@C anode electrode (labelled as AR@C). (g) Energy-dispersive X-ray spectroscopy (EDX) and elemental mapping analysis of top-view concave cavity-like sink surfaces of AR@C-shell dressers. The elemental mapping of AR@C composite of well-dispersed c-shell like layers along AR surface with percentage ratio 70.2:27.6:2.2% corresponding to O:Ti:C elements, respectively. (h) HR-TEM micrographs of AR@C convex mushroom-like surfaces of spherule-out-hollow, and circularly-shaped topography. (i) High-magnification HR-TEM pattern at lattice-edge showing a clear 3~4 nm-layer of C-shell layered-dressers along the entirely exterior coverage surfaces of AR@C convex mushroom-like surfaces. The inset of pattern (j) of the correspondent electron diffraction (ED) pattern [101]-TO crystal structure.

and (100) planes, respectively, of the [010]-dominated orthorhombic olivine LFPO structure in WG@C crystals. The HR-TEM image recorded at the edge of EG@C displays clear crystal planes with interatomic distances of 0.38 and 0.425 nm, which correspond to the (210) and (−101) planes, respectively. The crystal planes of the UG@C cathode obtained the d-spacing values of 0.38 and 0.348 nm, which correspond to the (210) and (111) planes, respectively. The plane arrangement in the lattice patterns of WG@C, EG@C, and UG@C spherule-rich gradients clearly show the formation of the orthorhombic LFPO structure. Figures 1(j) and Figures S1(h) and S2(i) present the selected area electron diffraction (SAED) pattern images of WG@C, EG@C, and UG@C, respectively, thus indicating that the [010] ac-plane is a prominent crystal facet along the G@C structures. The low surface energy of the [010] facet may lead to potential G@C cathode surfaces for rapid Li$^+$ ion diffusion and suitable accommodation.

Figures 2 (a–i) illustrate the images of low- and high-magnification FE-SEM and HR-TEM micrographs and EDX elemental analyses of top-concave and back-convex views of

spheroid-capped gradients in the 3D surface curvature agate rosettes (AR@C) of the anatase TO@C anode electrode. The convex orientation showed mushroom-like surfaces and structurally folded curvature concave surface models of cave-in-hollow nests and shell-walled/fenced edges with granules (200–600 nm in width size, 100 nm in depth, and 100 nm edge) abundant in ridges and grooves. The AR structural vehicle folds with a bundle of convex/concave spheroid-capped gradients create the dominant surface curvature as the force-driven modulation of high energy density and continuous electron/Li$^+$ ion transports during charge/discharge cycles. This type of electron/Li$^+$ ion transportation used the multi-diffusive open pore systems of the connective open macro-window and cage cavity along the entire interior/exterior of the AR spherical nests may offer large reversible capacity rate compared with other TO structures.[22,23] Figure 2(g) shows the elemental mapping of the AR@C composite with the percentage ratio of 70.2:27.6:2.2 for O, Ti, and C elements. Figure 1(D-b), SI Figures S1(D-b) and S2(f), and Figures 2(h–j) present the HR-TEM pattern images in the formation 3D surface curvature geodes (G-cathode)/agate rosettes (AR-anode) and the outer surface coverage by using the carbon-capped spheroid gradients with 3–4 nm of carbon-shell layers of WG@C, EG@C, and UG@C (G@C-cathode) and AR@C (anode) spherules. The anode//cathode electrodes are decorated by highly conductive C-shell layers, which can boost surface heterogeneity, 3D surface curvature function changes, and active surface dominants. These structural vehicle folds with a bundle of convex/concave spheroid-capped gradients, dominant surface curvature can facilitate electron/ion transports, enhance surface electronic conductivity, and increase the diffusion dynamics of electrons/Li$^+$ ions. Moreover, the encapsulation of the anode/cathode electrodes into the CR2032 coin cells may increase the integral electrode stability in half-scale anode/cathode and full-scale system AR@C//G@C LIBs. The well-coated layer with thermal stability and sustainable C-shell along circular-shaped anode/cathode topography occurring in the G@C cathode and AR@C anode was obtained by using thermogravimetric analysis, Fourier transform infrared spectra, Raman spectra, and X-ray photoelectron spectrometry (see Figures S4–S8).

Figures 3 and S9 show that the structural composite domains and structural ordering of circular-shaped spherule-rich WG@C, EG@C, and UG@C (G@C cathodes) and AR@C (anode) topographies were obtained by using X-ray diffraction (XRD) patterns. The XRD profiles of variable G@C cathodes exhibit well-defined peaks, which are indexed to the ordering spheroid-geode atomic scale, pure orthorhombic olivine-type LFPO structure and space group of standard spectra *Pnma* (JCPDS card No. 83–2092) (Figure 3A).[31] No significant change exists in the phase structures associated (such as Li$_3$PO$_4$, Li$_3$Fe$_2$(PO$_4$)$_3$-conductive FeP, or Li$_4$P$_2$O$_7$) with the LiFePO$_4$ pure phase. The Rietveld refinement results ($a = 9.814$ Å, $b = 5.817$ Å, and $c = 4.783$ Å, with an acceptable R_{wp} value of 1.238 and unit volume = 286.95 Å^3) are all in good agreement with the literature values (JCPDS card No. 83–2092).[29] The inset in Figure 3A illustrates the LFPO olivine crystal structure with [010] direction and possible lithium pathways. Figure S9 shows

the diffraction peaks of AR@C mushroom-like geode particles, indicating the tetragonal structure with the I4$_1$/amd space group. The XRD pattern of the AR@C anode indicates a formation of well-defined anatase structure (JCPDS 21–1272) in the absence of the phase crystal impurity of rutile and brookite structures. The AR lattice parameter values were calculated via refinement at $a = 3.789$ Å, $b = 3.789$ Å, and $c = 9.489$ Å of the TO. The XRD profile finding shows the atomic-scale arrangement of anode/cathode designs that can provide electron/Li$^+$ ion movement regulators along all the possible convex/concave surface curvatures, ridges, grooves, and low-energy top-in-plane surface sites. Figure 3B shows the N$_2$ isotherms of type IV with H$_2$ hysteresis loop for all G@C cathodes, indicating the formation of cave-in-hollow cages with uniform and connected pore cavities (Figure 3D-d). The S$_{BET}$ m^2/g value decreases in the order of WG > EG > UG spherule-rich geodes. Among the geode structures, the surface coverage of WG@C electrode has diverse surface functions similar to those of vehicle/truck storages, such as excellent specific capacities, facile charge-discharge rates, high energy density, and long timescale stability LIBs (Figures 3D[a–c]).

The key clues of the unique structures of AR@C-anode//G@C-cathode morphologies and 3D-reconstructed curvature surface variations are highlighted below (i.e., from i to iv items) to significantly synchronize the effectiveness of well-defined geometric anode/cathode electrode designs in the development and fabrication of full-scale LIBs.[32]

i. The formation of cave-in-hollow geodes (G)/agate rosettes (AR) may generate AR@C-anode//G@C-cathode electrode surface-like vehicle/truck storage with mesogrooves, meso/macrovoids, ridges, kinks, entrance windows/doors, and interior hollow-like nests in the core of mesospheroid- and cavity-like sinks (Scheme 1, Figure 3D and Scheme 2). These G-cathode//AR-anode electrode features offer a wide range of free-space accommodation for electron/ion occupation, high diffusion, dynamic mobility, and continuous electron-ion motion systems during the lithiation/delithiation process.

ii. The 3D spherule-rich interstitial G/AR surface model with a bundle of convex/concave spheroid-capped gradients, remarkable surface curvature function changes, and circularly-shaped topographic dominants differentially regulate the G@C-cathode//AR@C-anode as vehicle folds for the force-driven modulation of the high energy density of LIB-EV.

iii. The single-crystal structure with heterogeneous composites, lithium-rich surface sites along the central crystal and upper zones of the top surface of the atomic-scale arrangement of the G-cathode/AR-anode (Figures 1D, 2 h-I and 3 A) enabled the mounting of surface functions in the electron/ion diffusion with multiple charge/discharge cycles, directional gates, highly dense sites, and small electron transport distances, thereby increasing the multi-diffusible ions in the electrode surfaces within the formulation of well-defined geometric half- or full-cell LIBs.

iv. Among all the cathodes used in built-in full-scale LIBs, the high-index exposed surfaces and crystal interfaces, and
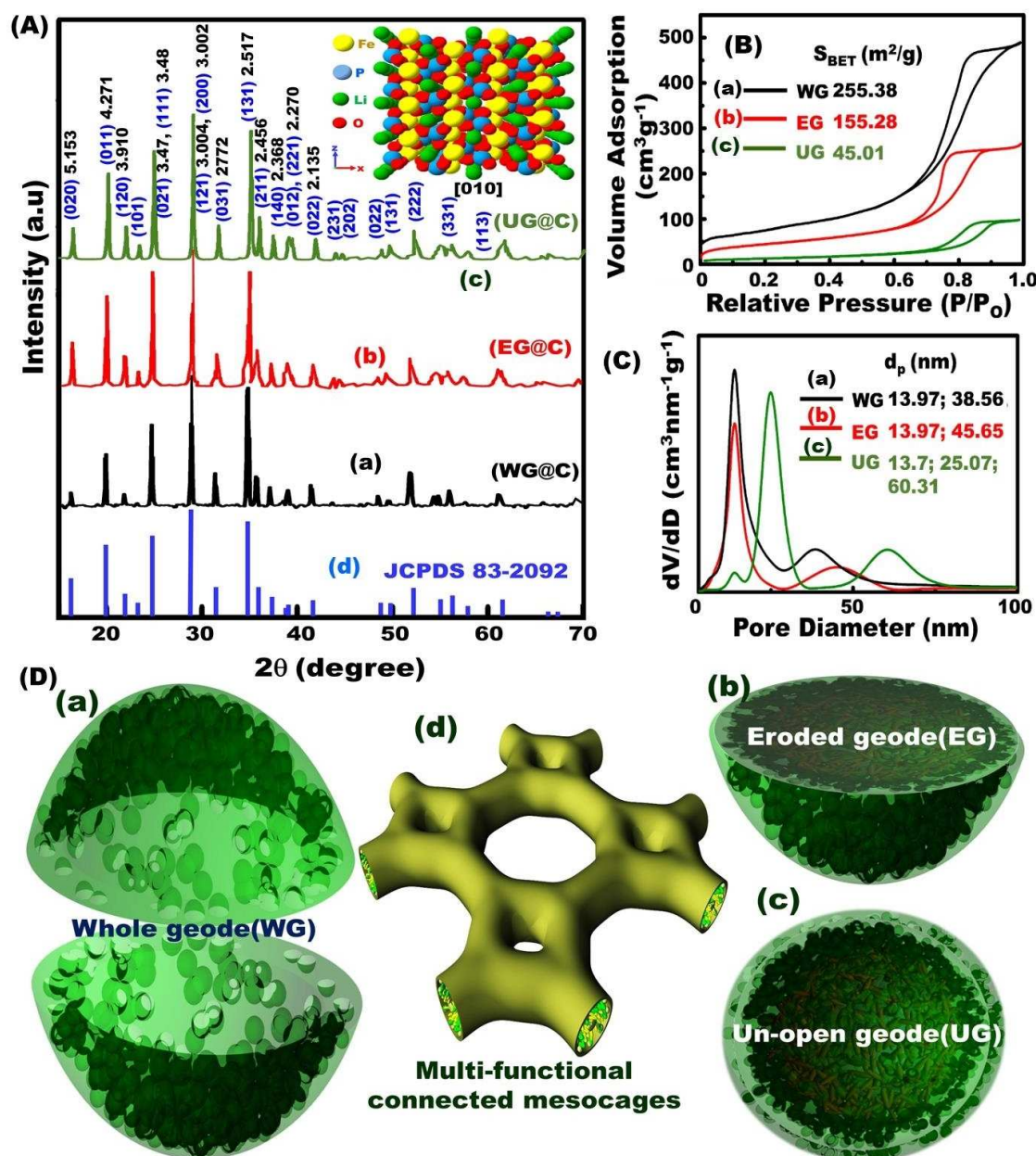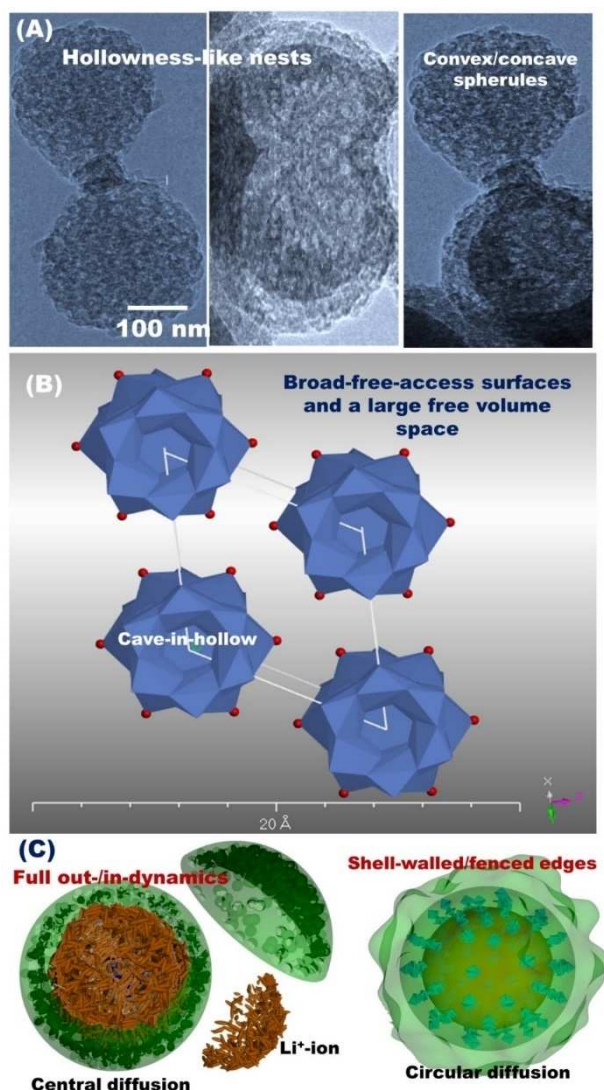
Figure 3. (A) XRD patterns, (B) N_2 isotherms, (C) pore size distribution, and (D) 3D reconstructed objects along structurally-folded curvature surface models designated with cave-in-hollow, shell-walled/fenced edges, and convex/concave spheroid-capped gradients of 3D-surface curvature geodes (G-cathode) with whole open (WG@C), eroded (EG@C) and unopened (UG@C) spherules. Inset (A) is the crystal structure of olivine-geode cathodes (olivine-whole geodes-like structure particles included WG@C in the direction [010] and possible lithium orientation pathways. Inserts (B and C) are the surface areas in m^2/g and the corresponding pore-size distribution curves (D-a-D-d) 3D topographic projects showed top- and aside views of G-cathode vehicle/truck storages. (D) The projection regularities showed structural vehicle folds with a bundle of open cave-in-hollow, shell-walled/fenced edges, and convex/concave spheroid-capped gradients oriented in the whole circularly-shaped topography (Da-d).

uniquely spherule-rich interstitial core cavity-like sinks with wide curvature surface folds of WG@C may produce the extra active ion transportation in 3D surface curvature geodes (G) into Li^+ ion diffusion sites via upstream swirls and multi-diffusivity in convex/concave directions. The WG@C mesospheroids may be a promising candidate in EV applications as a cathode because it can meet the high power and energy requirements of LIBs.

Figures 4–7 show that the electrochemical performance of half-scale vehicle/truck storages based WG@C, EG@C, and UG@C cathodes were specifically studied to demonstrate the key fabrications of the cathode//anode design in the formulation of built-in full-scale LIB vehicle/truck storages based on AR@C-anode//G@C-cathode composites. In addition, the electrochemical performance of the half-scale AR@C LIB anode vehicle/truck storages was examined to control the development of the full-scale G@C-cathode//AR@C-anode LIB modules

Scheme 2. Microscopic HRTEM studies (A) and density functional theory (DFT) projections of upward anode geode hollowness gradients (B), and unique structures of cathodic geode morphologies with full-open-capped geodes (C) oriented after charge/discharge cycles. The retention of structurally-shaped vehicle/truck storages along anode//cathode surface curvature dominants, leading to multi-diffusible dimensions, and massive way-in-transport of electron/Li$^+$-ion diffusion during the lithiation/delithiation process.

with outstanding energy density as a promising model for energy storage applications, particularly in EVs (see SI Figures S10 and S11).

2.2. Half-CR2032 Coin Cells based on G-Cathode LIB Vehicle/Truck Storages

The building design of half-scale CR2032 coin cells with spherical G-cathode LIBs with 3D-reconstructed curvature surface variations used with structurally shaped spheroids in WG@C-, EG@C-, and UG@C-cathode geode dominants was formulated to measure its electrochemical performance and

function similar to those of vehicle/truck storages (see Figures 4–7).

Figure 4(a) exhibits the typical 1st cyclic voltammogram profiles of prepared half-scale CR2032 coin cells with spherical G-cathodes (i.e., WG@C, EG@C, and UG@C morphologies) within the potential region of 2.0–4.3 V versus Li/Li$^+$ at a scan rate of 0.1 mV/s. Note that the same mass fraction of all G-cathode-active materials is applied for fabrication of half-scale CR2032 coin cells. The reduction/oxidation peaks of WG@C, EG@C, and UG@C were obtained at 3.12/3.61, 3.07/3.69, and 3.02/3.75 V, respectively. Figure 4(b) shows the CV curves of WG@C cathode for the 1st cycle at different scan rates of 0.1, 0.5, 1, 5, and 10 mVs^{-1} within a potential range from 2.0 V to 4.3 V. The voltage values in the oxidation and reduction peaks increased and decreased with the increasing scan rate, respectively. The absolute current values also increased in the oxidation and reduction peaks with the increasing scan rate. Figure 4(c) shows the cyclic stability of WG@C cathode in the 1st, 10th, 50th, 100th, and 200th cycles at a sweep rate of 0.1 mVs^{-1} within a voltage range from 2.0 V to 4.3 V. The symmetric peak figuration for Fe^{2+}/Fe^{3+} can be observed easily at 3.12/3.61 V for the WG@C cathode within cycles. The symmetric behavior indicates excellent reversibility along our designated vehicle/truck storages during the electrochemical process of Li$^+$ insertion (cathodic, reduction, lithiation)/extraction (anodic, oxidation delithiation), respectively (Scheme 1). The significant coincidence of the CV curves during the charge/discharge process is attributed to the excellent cycling performance and high reversible capacity of WG@C for 200 cycles.

The charge-discharge cycling performance profiles presented in Figure 5 were examined to investigate the effect of the structural vehicle folds of geodes (G@C-cathode) with variable geometric models of WG@C, EG@C, and UG@C spherules on the electrochemical performance of half-scale G-cathode LIBs. Figure 5(a) exhibits the 1st charge-discharge cycle of WG@C, EG@C, and UG@C half-cell cathodes for different hierarchical structures within the potential region of 2–4.3 V versus Li/Li$^+$ at the current rate of 0.1 C. The G@C-cathode cells were charged to 4.3 V at 0.1 C, kept at 4.3 V for 1 h, and then discharged to 2.0 V at 0.1 C. The WG@C cathode shows the highest storage capacity among all the EG@C and UG@C cathode structures. The half-scale CR2032 coin cell with WG@C cathode exhibits a significant discharge capacity of 168.3 mAh g^{-1} for the 1st cycle, which is higher than that of both the EG@C and UG@C cathode discharge capacity values at 149.1 and 128.2 mAh g^{-1} at 0.1 C, respectively. The highest discharge capacity of WG@C cathode may be attributed to uniqueness of the curvature surface folds with whole open geodes and multiple wide-mouthed caves thereby generate functions similar to those of vehicle/truck storages. The WG@C cathode vehicle folds provide evidence of the massive gate-in-transport of Li$^+$ ion diffusion in the empty mesocage-in caves and enlarged diffusion entrance voids and windows via the lithiation/delithiation process compared with other G-cathode models. Figure 5(b) presents typical 1st cycle charge/discharge curves of WG@C as the cathode electrode in half-cell LIB vehicle/truck storages at various scan rates of 0.1, 0.2, 0.5, 1, 5,
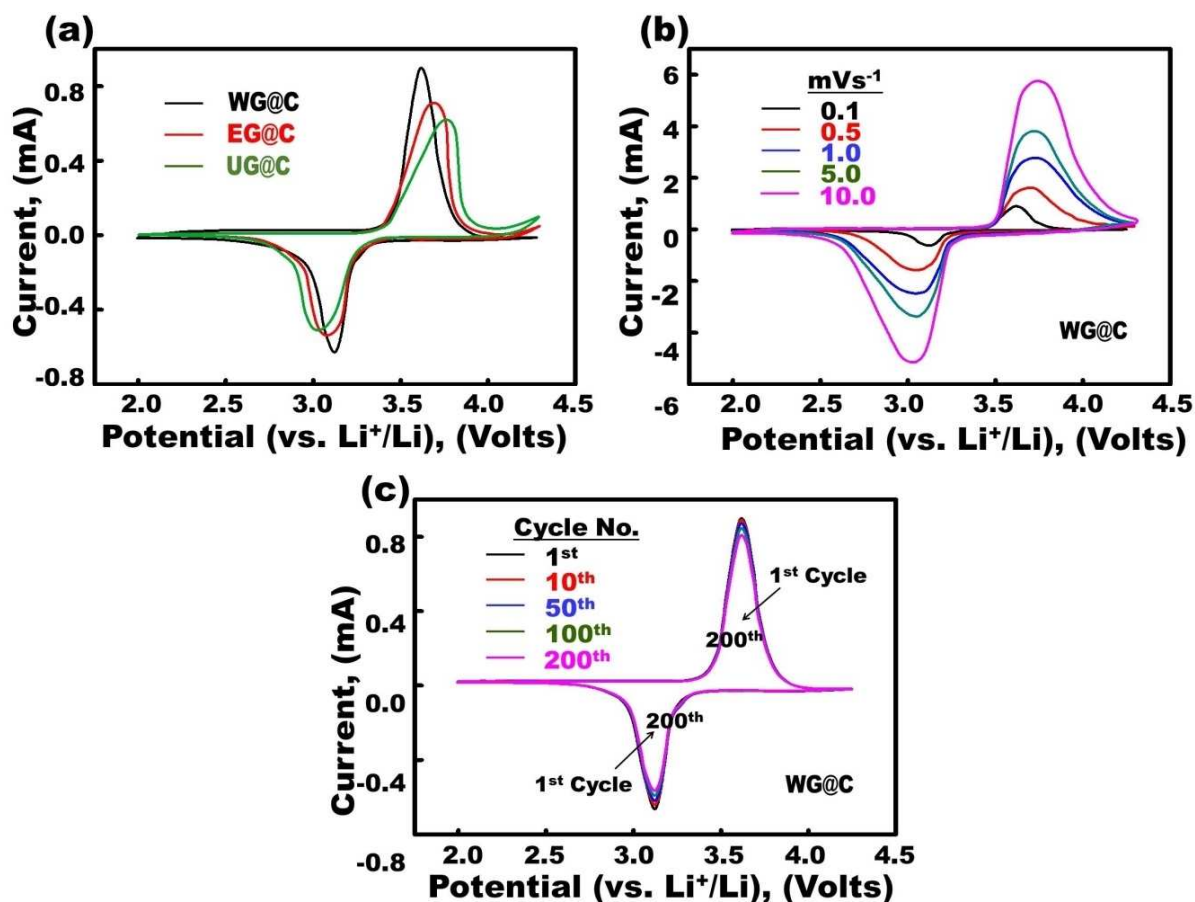
Figure 4. Study the effect of structural vehicle folds of geodes (G@C-cathode) with whole open (WG@C), eroded (EG@C) and unopened (UG@C) spherules on the electrochemical performance of half-scale G-cathode LIBs. (a, b and c) Cyclic voltammograms and comprehensive analysis of the electrochemical performance of the cathode composites (2032 coin-type half-cell tests with a Li counter electrode). (a) CV curves of different structures of 3D reconstructed curvature surface variations oriented with structurally-shaped spheroids along WG@C, EG@C and UG@C cathodes. (b) CV curves of WG@C half-cell cathode at different sweep rates of 0.1,0.5,1,5 and 10 mVs^{-1} (c) CV curves of WG@C half-cell cathode at different cycle numbers from 1–200 cycles at 0.1 mVs^{-1}. All electrochemical measurements for half-cell G@C cathodes were operated within voltage range of (2.0–4.3 V), at room temperature.

10, and 20 C in the voltage window of 2.0–4.3 V versus Li/Li$^+$. Figure 5(b) demonstrates that the WG@C cathode with whole open cave geodes and highly exposed curvature surfaces exhibits excellent behavior with its high discharge capacity at the extensive current C-rates from 0.1 C to 20 C compared with that of half-cells prepared for other G-cathodes, such as EG@C and UG@C. Figure 5(c) clearly illustrates the charge/discharge curves of the WG@C cathode model half-cell LIBs at different cycle numbers (1st, 2nd, 20th, 50th, and 100th cycles). This finding emphasizes the formation of real WG@C LIB vehicle/ truck storages with outstanding long-term cycling performance. The WG@C topographic functions as vehicle/truck storages can be ascribed to the time-scale stability of the diffusion dynamics of electrons/Li$^+$ ions through multiple transport gates such as open cave-in-hollow nests, spherule-rich interstitial core cavity-like sinks, and circularly-shaped orientations, despite the long lithiation/delithiation cycling processes.

Figure 6 shows that the structural vehicle/truck folds of geodes demonstrated significant influence on the discharge capacity and cycling performance stability of the building design of half-scale CR2032 coin cells with spherical G@C-cathode LIBs. For example, Figure 6(a) shows the 1st discharge capacity for WG@C, EG@C, and UG@C half-cells cycled at several scan rates of 0.1–20 C between 2.0 and 4.3 V versus Li/ Li$^+$ at a scan rate of 0.1 mV/s. The 1st discharge capacity values clearly decrease in this order: WG@C > EG@C > UG@C cathode spherules at overall scan rates. The superior retention in cycling performance and long-term cycle stability of current G@C-cathode LIBs is clearly noticeable in Figure 6(b). For instance, the WG@C cathode reached 97.50 % of its 1st cycle capacity after 100 cycles at (1 C), whereas 96.15 % and 90.64 % were retained after 100 cycles for EG@C and UG@C cathodes from their initial capacities, respectively. The low capacity fading of the half-cell WG@C cathode design at the 100th cycle at the rate of 1 C compared with that of other EG@C and UG@C cathode models can be attributed to the primary tectonic structures as follows: (i) structural geode robustness in terms of vehicle/truck storage loads; (ii) sustainability of full Li$^+$ ion in/out dynamic mobility; (iii) massive way-in-transport of electron-ion motion systems; and (iv) rapid Li$^+$ ion transfer kinetics, leading to high
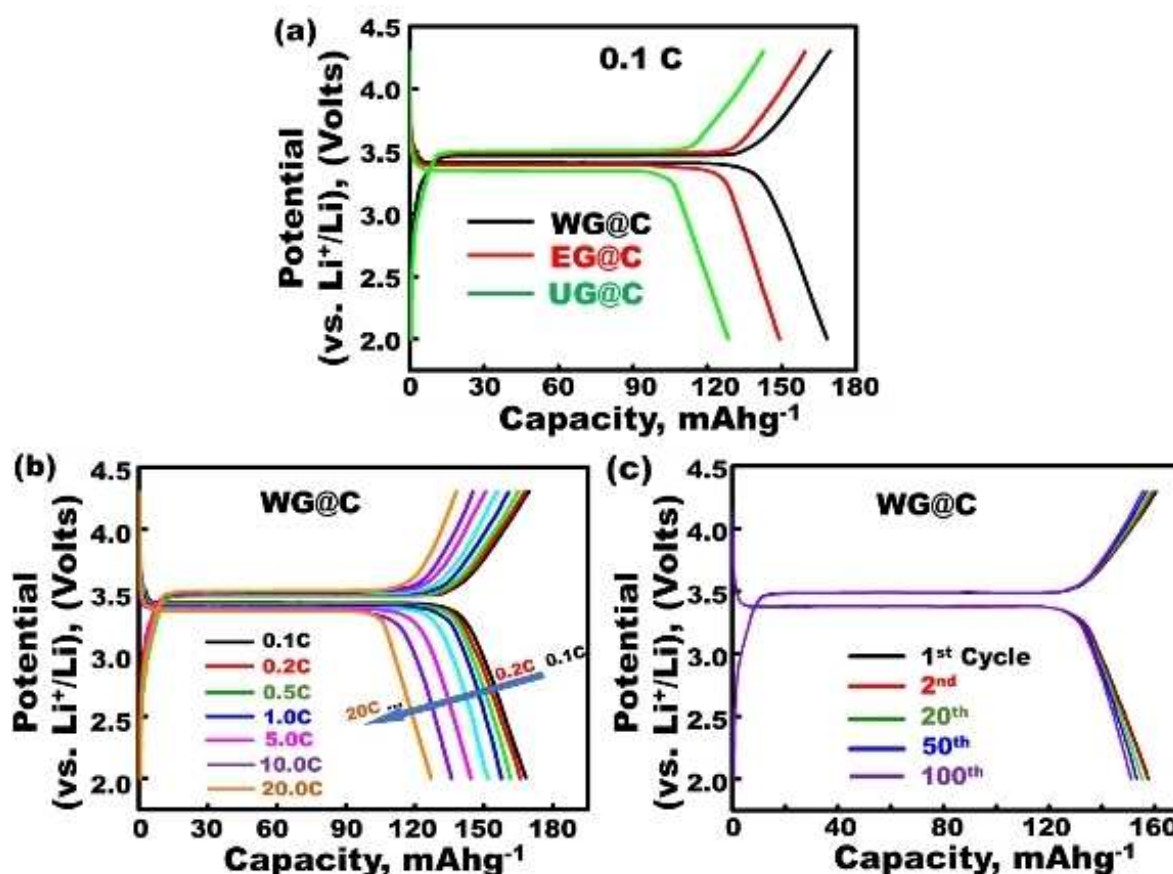
Figure 5. (a-c) Effect of variable model G@C-cathode geometrics as vehicle/truck storages on rates and cycling behaviour during the charge-discharge voltage profiles. (a) First cycle half-cell cathodes of WG@C, EG@C and UG@C cathodes at current rate 0.1 C (b) First cycle half-cell WG@C cathode at different current rate from 0.1 C to 20 C (c) The whole open geode WG@C as half-cell cathode at a current rate 1.0 C at different cycle number up to 100 cycles. All electrochemical measurements were operated at room temperature.

electrochemical reversibility during lithiation/delithiation processes with half-cell WG@C cathodes.

The capability performance rate of structurally folded curvature surface models designated with half-the cell G@C-cathode was investigated in the LIB design (Figure 7a). The cycling performance of 3D surface curvature geodes (G@C-cathode) was tested at different rates (0.1, 0.2, 0.5, 1, 2, 5 C and back to 0.1 and 10 C, and then back to 1 and 20 C with 10 cycles at each rate) for the prepared WG@C, EG@C, and UG@C at room temperature. Figure 7(a) shows that the specific capacity decreases with the increasing current rate for all G@C-cathode models. Among these models, the WG@C cathode exhibits a remarkable and surprising performance advantage of outstanding rate capability and long cycle stability with high volumetric energy density over the different C-rates within 1–100 cycles. The excellent reversible discharge capacity of the WG@C cathode model is approximately 124.3 mAhg^{-1} at the rate of 20 C after 100 cycles, whereas that of other prepared EG@C and UG@C cathode models significantly decreased during repeated Li intercalation at 77.5 and 8.5 mAh g^{-1} at the rate of 20 C after 100 cycles, respectively. The effect of the open cave-in-hollow nests, spherule-rich interstitial core cavity-like sinks, and circularly-shaped topography on the electro-

chemical performance of the half-scale CR2032 coin cells built with variable G@C-cathode LIB vehicle/truck storages was further tested via electrochemical impedance spectroscopy (EIS). Figure 7(b) illustrates the Nyquist plots obtained from EIS for WG@C, EG@C, and UG@C as half-cell cathode models. These Nyquist graphs form a semicircle and a slanted line at the high- and low-frequency regions, respectively. The inset in Figure 7 (b) shows that the EIS results can be illustrated based on the equivalent circuit. The equivalent circuit of half-scale CR2032 coin cells built with variable G@C-cathode LIBs consists of electrolyte resistance (R_s, the intercept impedance on the real axis corresponding to the solution resistance), charge-transfer resistance (R_{ct}, caused by the electrochemical interaction at the G@C-cathode electrode/electrolyte interface and particle/particle contact), constant phase element, and Warburg impedance of Li$^+$ ion diffusion into the G@C electrode (W_f, related to the low-frequency region of the straight line).[33,34] The semicircular arc at the highest frequency range is relative to the R_{ct} value. R_{ct} is approximately equal to the numerical value of the diameter of the semicircle on the Z real axis. The smallest semicircle diameter and minimum R_{ct} value WG@C compared with those of other G@C cathode models indicate the massive gate-in-transport of the electron/Li$^+$ ion and rapid electron/ion
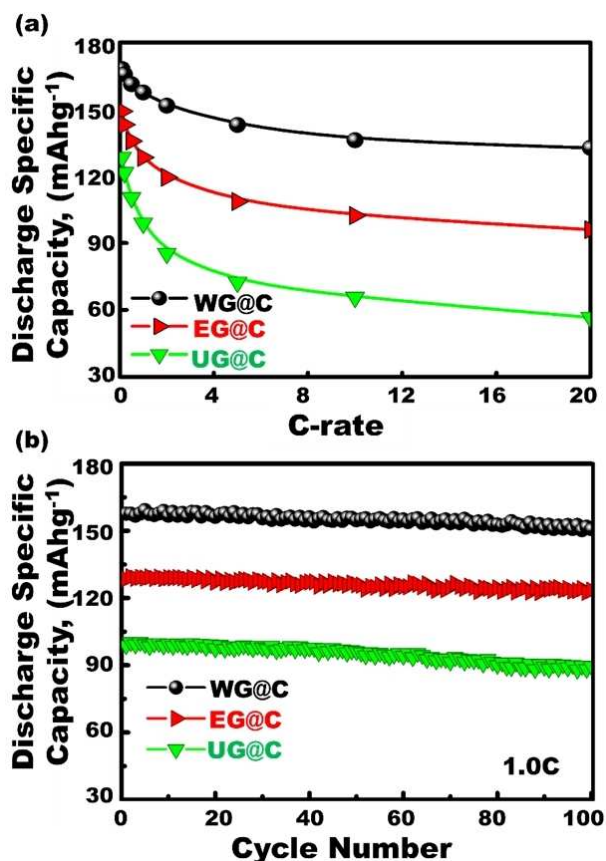
Figure 6. (a,b) Influence of structural vehicle folds of geodes (G-cathode) with whole open (WG@C), eroded (EG@C) and unopened (UG@C) spherules on first discharge capacity (a) and cycling performance stability (b). (a) First discharge capacity recorded at a current rate 0.1 C–20 C of half-cell G@C-cathode LIBs. (b) Cycling performance stability for used WG@C, EG@C and UG@C cathodes in half cell 2032-coin cell with Li-foil as counter electrode, at rate of 1 C for 100 cycles. All electrochemical measurements for half-cell G@C cathodes were operated within voltage range of (2.0–4.3 V), at room temperature.

transfer kinetics of the WG@C cathode during lithiation/delithiation processes. Furthermore, the carbon-capped spheroid gradients with an approximate size of 3–5 nm along 3D surface curvature geodes (G@C-cathode) assist in the electron/ion transportation kinetics across the heterogeneous components and interfaces of geode particles during lithiation/delithiation processes and enhance the superb electronic conductivity and surface transport functionality.[35]

The anisotropic building components of the G@C-cathode with C-shell layers in spherule-rich interstitial core cavity-like sinks and circularly-shaped topography of geode dominants play an important role to enhance the Li$^+$ ion diffusion, improve the sustainability of the atomic-scale arrangement, and protect the electrode building layers from degradation against temperature and multiple charge/discharge cycles. The evidence on the significant workability of half-scale CR2032 coin cells built with variable G@C-cathode LIBs at different temperature ranges was clearly investigated (Figure 7c). Figure 7(c) compares the temperature dependence functionality and electrical conductivity of 3D-reconstructed curvature sur-

face variations with structurally shaped spheroids along WG@C, EG@C, and UG@C half-cell cathodes. The significant surface curvature function changes in well-defined geometric G@C-cathode LIBs exhibit good conductivity at room temperature (298 K). The WG@C cathode showed excellent conductivity in the tested temperature range (approximately 250–455 K) among all G@C cathodes.

2.3. Anodic Half-Cell Built-in LIB-based 3D Surface Curvature AR@C Spherule Models

The electrochemical performance of the half-cell AR@C anode as vehicle/truck storages in the LIB design (see Supporting Information S1) was studied to explore the effectiveness of structurally folded curvature surface models, which used the AR@C-electrode as the potential anode LIB model. Figure S10 (a) shows the charge-discharge potential curves of the 1st cycle at the different rates of 0.2, 1, 5, 10, and 20 C for the half-cell AR@C anode structure. The galvanostatic charge/discharge profiles of the AR@C anode in half-cell LIB configurations are investigated in the voltage region from 1 V to 3 V versus Li/Li$^+$. Each discharge characteristic curve is divided into three plateau bands. First, the steep sloppy region of discharge is caused by the formation of the solid solution (an insignificant quantity of Li$^+$ ions are inserted in the AR@C electrode) and determined with the rapid plateau slope potential from the open circuit voltage (OCV of approximately 3 V) at ca. 1.7 V versus Li. Second, the discharge zone is a long distinct flat plateau at ca. 1.7 V due to the lithiation in approximately half of the vacant octahedral positions of the anatase TO structure (Figure S9, inset). Third, the discharge stage displays a gradual decrease in the potential after the plateau zone-like knee at 1.7 V to the cut-off voltage at 1.0 V versus Li. This phenomenon can be attributed to anodic vehicle/truck storages in terms of massive gate-in-transports and Li$^+$ ion loads into geode gradients of the AR@C surfaces (i.e., the formation of interfacial/interstitial core pocket storage). The charge profiles also form three regions. The first shows the increase in capacity from 1 V to 1.96 V due to the monotonic delithiation process, which is directly followed by the second region of the continued Li$^+$ extraction process in the plateau regime. Finally, the third region in the curved solid solution regime tending toward 3.00 V was distinct. Figure S10b illustrates the specific capacity values of the 1st cycle discharge of the half-cell AE@C anode at several current rates ranging from 0.2 C to 20 C. Figure S10c shows the Nyquist plot based on the EIS results of structurally folded curvature surface models with the designated half-cell AR@C anode.

Figure S11 presents the rate capability performance in the range of 1.0–3.0 V for the AR@C anode electrode at the different rates of 0.1, 0.2, 0.5, 1, 2, 5 C and back to 0.1 and 10 C, and then back again to 1 and 20 C with 10 cycles at each rate after 100 cycles at room temperature. The rate capability result shows that the specific capacity of the half-cell AR@C anode decreases with the increasing current rate. In addition, the capacity of the half-cell AR@C anode significantly decreases
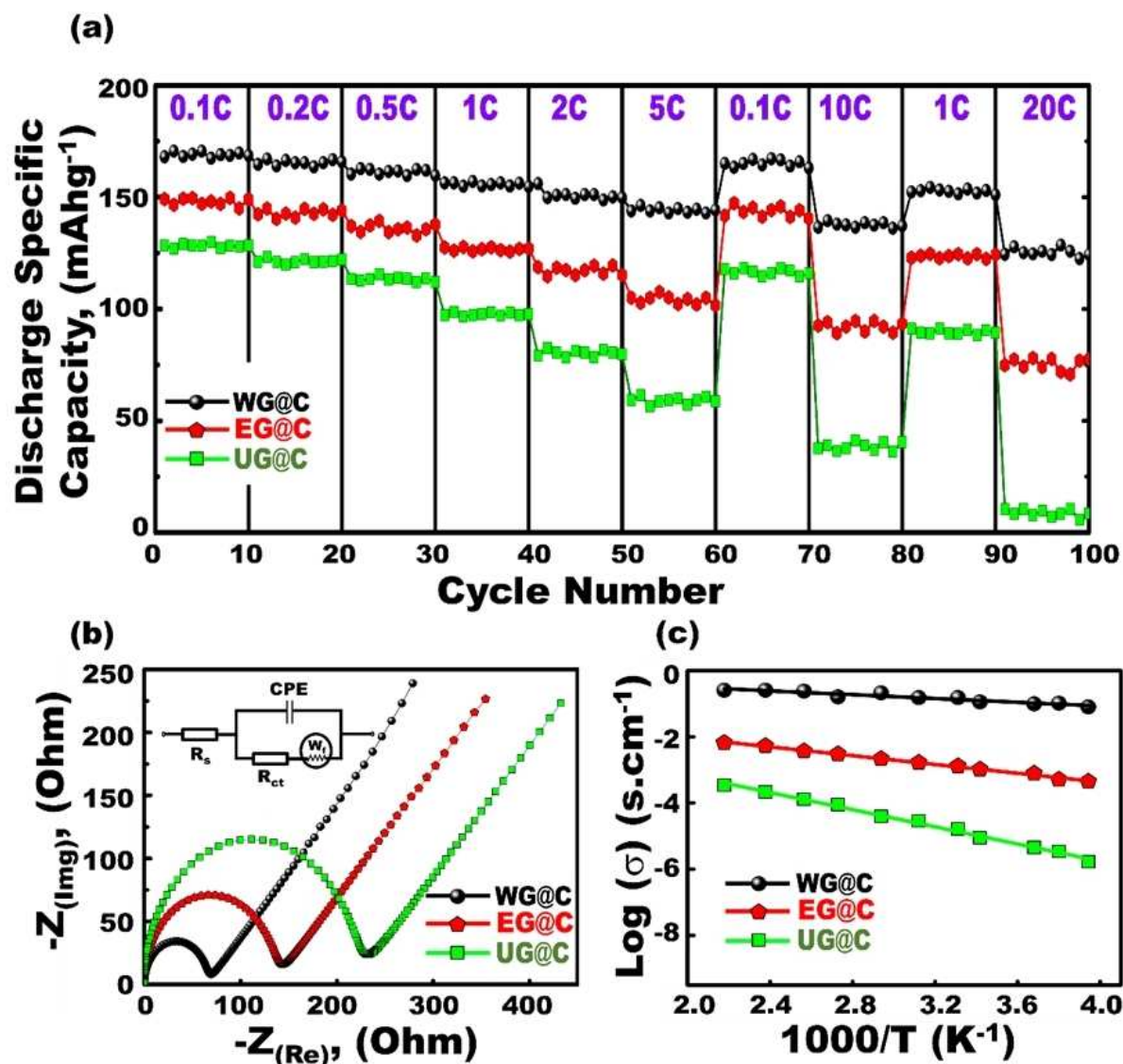
Figure 7. (a-c) Electrochemical performance of the half-cell G@C cathode build-in-LIB formulated with 3D reconstructed curvature surface variations oriented with structurally-shaped spheroids along whole-, eroded- and non-opened geode dominants (WG@C-, EG@C- and UG@C-cathodes, respectively). (a) Capability performance rates over a range of 2.0–4.3 V among G-cathode geodes: WG@C, EG@C and UG@C at various current rates from 0.1 C to 20 C. (b) The electrochemical impedance spectroscopy (EIS) results of prepared C-coated cathode materials of different morphologies. (c) Temperature dependence comparison of electrical conductivity for different structures of prepared C-coated cathode materials of different morphologies. All electrochemical measurements for half-cell anodes were carried out at room temperature.

during the repeating Li intercalation process at 99.1 mAh g^{-1} and a rate of 20 C after 100 cycles. This finding indicates the effect of anodic AR@C vehicle/truck storages with a bundle of convex/concave spheroid-capped gradients, and dominant surface curvature for long-term charge/discharge cycles, and outstanding discharge capacities.

2.4. Full-Cell Vehicle/Truck Storages of WG@C//AR@C Integration for High-Energy LIBs

Scheme 1 shows the full-scale LIB building design of G-cathode//AR-anode LIB vehicle/truck storages with open cave-in-hollow nests, spherule-rich interstitial core cavity-like sinks,

and circularly-shaped topography. This illustration is the first evidence of the structural curvature effect of cave-vehicle/truck folds with a bundle of convex/concave spheroid-capped gradients on the creation of the anode/cathode design as the force-driven modulation of high energy density of full-scale G-cathode//AR-anode LIBs. The key values of high electrochemical performance experiments of designated half-cell-based AR@C (anode) and WG@C (cathode) in LIB designs (Figures 4–7 & Figures S10–S11) guided the formulation of the anode//cathode in full-scale hybrid LIBs.

A powerful built-in LIB anode/cathode vehicle/truck storage was designated in 2032 coin-type full-scale model tests. In this vehicle/truck storage design, G@C-cathode//AR@C-anode materials were loaded on Al- and Cu- foil as counter electrodes,

respectively, under supreme electrochemical performance conditions for the first time (Figures S1). Our full-scale, heterogeneous $LiFePO_4$ G-cathode//TiO_2 AR-anode pouch LIB-model was designed with a number of stacked layers of G-cathode, which are equal to 6-layers with 10 sides loaded on Al-foil (10 μm) (P) positive collector. In turn, the number of stacked layers of AR-anode is equal to 5-layers with 10 sides loaded on Cu-foil (8 μm) (N) negative collector (See Supporting Information S1). The building blocks of WG@C//AR@C cathode//anode full-scale LIB-vehicle folds were designated under optimized mass loading of negative AR-anode and positive G-cathode electrode (i.e., capacity balancing of (N/P)$_{cap}$ ratio). The optimization of full cell (balancing) (N/P) ratio, full-scale cathode//anode stacked layers pouch LIB-model, mass loading, areal capacity and volumetric energy density was controlled to built-in LIB vehicle/truck storage. The mass loading is 13.5 mg/cm^2 and 7.2 mg/cm^2 of cathode and anode active materials. Moreover, the areal discharge capacity is 1.13 Ah/cm^2 and 1.19 Ah/cm^2 for the cathode and anode electrodes, respectively, indicating a general balancing based on the assumption that discharge specific capacity (in Ah) is equal for negative and positive electrode, giving the inevitable control on (N:P)$_{Cap}$ capacity ratio with 1:1 value. In this LIB vehicle/truck storages, we control the built-in-LIB design on the base of the optimal trade-off key demands, which offer rational scale up with maintaining relationship between (i) the better safety (i.e., oversizing of negative electrode capacity, and the (N:P)$_{Cap}$ capacity ratio => 1:1), and (ii) optimum specific energy (i.e., reaching to equal capacities at N-anode and P-cathode electrodes with (N:P)$_{Cap}$ capacity ratio = 1:1). Thus, the proposed $LiFePO_4$ G-cathode//TiO_2 AR-anode stacked layers of pouch LIB vehicle/truck storage is fabricated under optimized mass loading (N:P)$_{Cap}$ ratio of ≈1.01–1.1:1 (Table S1 and S12). Furthermore, the mass% of the WG@C-cathode in the full-scale LIB cell is approximately 45% of the entire mass used for AR@C-anode//WG@C cathode built-in electrode sets, according to the estimated mass fraction of individual pouch full-cell-model components (Table S1).

The specific discharge capacity in mAhg^{-1} versus current C-rates from 0.1 C to 20 C for designated full-cell WG@C//AR@C (Figure 8(a)) was investigated to demonstrate the key role of vehicle/truck folds and their surface functions such as (i) cave-in-hollow nests, (ii) shell-walled/fenced edges, (iii) degree of 3D surface curvature, and (iv) convex/concave spheroid-capped gradients in the design of LIBs (Scheme 2). The structurally folded curvature surface anode/cathode LIB models showed excellent discharge capacity in the different ranges of current rates at 0.1, 0.2, 0.5, 1, 2, 5, 10, and 20 C between the voltages of 0.8 and 3.5 V. Figure 8a shows the gradual decrease in the discharge capacities with increasing C-Rate, resulting in the gradual decrease from 169.6 mAhg^{-1} at 0.1 C to 137.5 mAhg^{-1} at 20 C. This finding indicates that the powerful AR@C-anode//WG@C cathode built-in electrode sets provide excellent energy density at 292.5 Whkg^{-1} for the $LiFePO_4$ (WG@C) cathode. The quantity-based mass fraction of the cathode//anode affected the development of the high energy density full-scale LIB design. For example, the mass% of the WG@C-cathode in the full-scale LIB cell is approximately 45% of the entire mass used

for AR@C-anode//WG@C cathode built-in electrode sets (Table S1). Accordingly, the specific energy density values for the WG@C P- cathode//AR@C N-anode) full-scale LIB vehicle/truck storages were 131.6 and 143 Whkg^{-1}, according to the practical and theoretical investigations (see Supporting Information S12), supporting the driving range requirement for EVs. To explore the preferable design shape for large scale LIB- vehicle/truck storages of our proposed AR@C//WG@C full-scale system, we have estimated volumetric energy density of our models. The finding indicates that 18650-cylindrical-shaped model as a preferable design more than that pouch cell to approve the low cost, high energy density full-scale LIB vehicle/truck storages (see Supporting Information S12).

A set of experimental evaluation methods on the capability performance rates in the range of 0.8–3.5 V of half-cell and full-scale built-in WG@C//AR@C (cathode//anode) LIB models were examined at different C-rates (0.1, 0.2, 0.5, 1, 2, 5 and back to 0.1 and 10 C, and then back to 1 and 20 C with 10 cycles at each rate of up to 100 cycles at room temperature (Figures 8b and 8c)) to determine the influence of the building design of full-scale WG@C-cathode//AR@C-anode LIBs as vehicle/truck storages on the development of high energy density compared with that of half-cells of WG@C-cathode and AR@C anode LIBs. In all half-cells and full-scale LIB models, the specific discharge capacity decreases with the increasing current rate. However, the full-scale built-in WG@C//AR@C (cathode//anode) LIB model showed the highest retention at the original discharge capacity/mAhg^{-1} despite the wide range of C-rate at 0.1–20 C or multiple cycles compared with that of half-cells of WG@C-cathode and AR@C anode LIBs. The full-scale built-in WG@C//AR@C cycling performance of 1 C (i.e., at 40 cycles) and 5 C (i.e., at 60 cycles) returned to 1 C (at 90 cycles) and 20 C (at 100 cycles), thereby indicating to the retention of ≥97% from its initial specific capacity. This finding indicates that the structurally folded curvature surface anode//cathode electrodes used as vehicle/truck storages with cave-in-hollow nests, shell-walled/fenced edges, and convex/concave spheroid-capped gradients may lead to efficient full-scale built-in WG@C//AR@C (cathode//anode) LIB models with a high value of specific energy density and outstanding rate capability (Scheme 1).

Figure 9 (a, b) proves the effectiveness of the building design of full-scale spherical WG@C-cathode//AR@C-anode LIBs in the creation of vehicle/truck storage loading for massive gate-in-transport of electron/Li^+ ion for long-term charge/discharge cycles, outstanding discharge capacities, and Coulombic efficiency at a rate of 1 C of up to 2000 cycles in the potential region from 0.8 V to 3.5 V versus Li/Li^+ at room temperature. In general, the proposed structurally folded curvature surface WG@C//AR@C full-cell LIB model shows excellent cycling behavior, operating at 1 C rate with 85% discharge capacity retention even after 2000 cycles (see Figure 9). The Coulombic efficiency of WG@C//AR@C LIBs was 92% at the first cycle. In fact, the formation of solid-electrolyte interphase (SEI) film at negative AR@C anode is a key factor to this initial irreversibility loss and then leading to 8% capacity fading.[36,37] Within 20 cycles, the Coulombic efficiency increases to ≥99.5%, and then attained its potential value ~100% up to
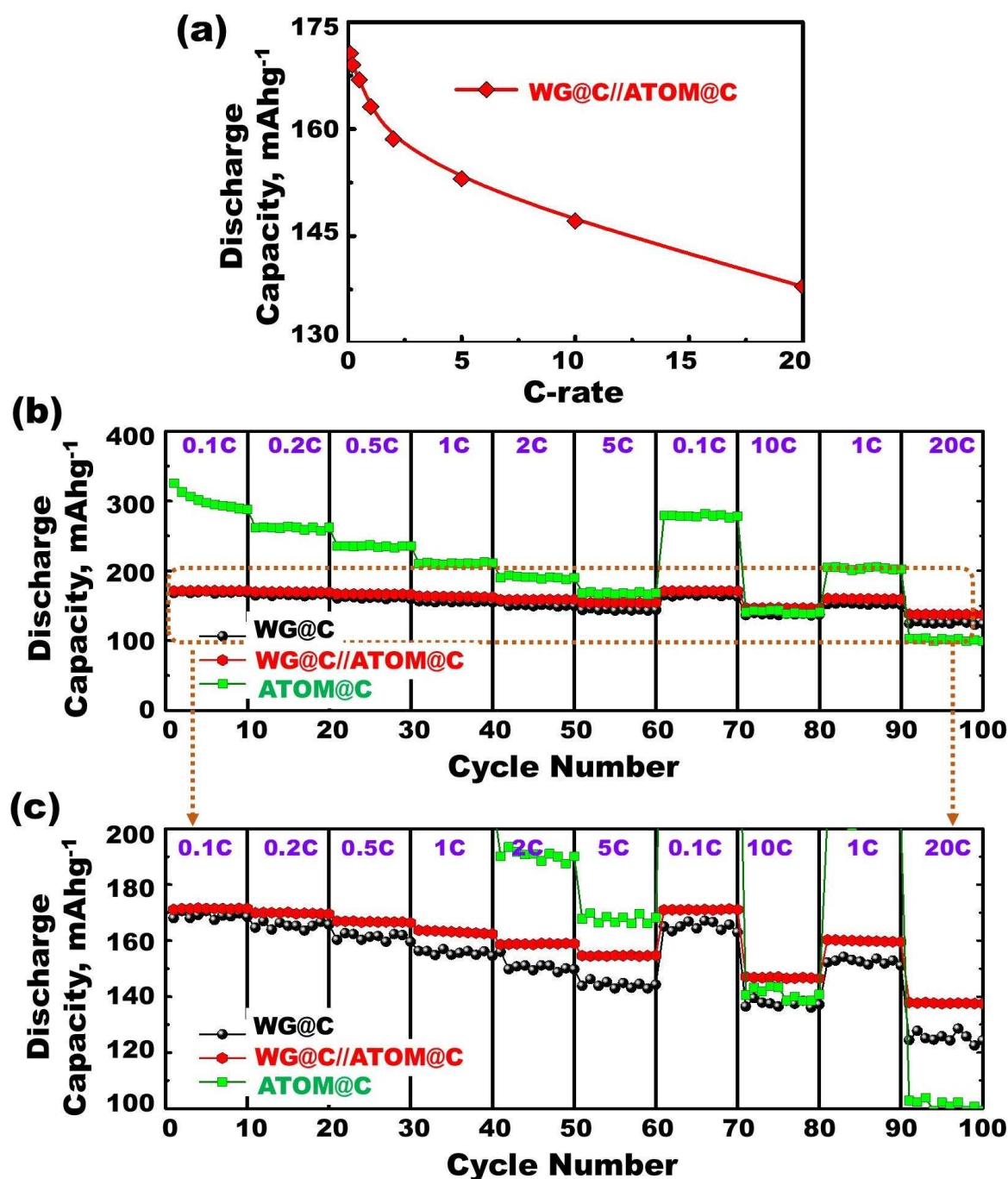
Figure 8. Study the influence of the building design of full-scale spherical G-cathode//AR-anode LIBs on the development of high energy density full-scale LIB design compared with both half-cell G@C cathode and AR@C anode LIBs designated in half cell 2032-coin cell with Li-foil as counter electrode and with Cu- and Al-foils as counter electrodes in the case of full-scale G@C-cathode//AR@C-anode LIBs, respectively. (a) Performance of specific discharge capacity in mAhg^{-1} versus current C-rates at 0.1 C, 0.2 C, 0.5 C, 1 C, 2 C, 5 C, 10 C and 20 C, and between voltage of 0.8 and 3.5 V for powerful WG@C(cathode)//AR@C (anode) full-scale LIB-model. (b) Performance and behavior of the rate capability of WG@C//AR@C full-scale LIB-model over a range of 0.8–3.8 V at various current rates from 0.1 C to 20 C. (c) Enlarged the selected part of (b) for rate capability performance results of spherical-geodes built-in WG@C//AR@C full-scale LIB-model. All electrochemical measurements were operated within voltage range of 0.8–3.5 V at 25 °C.

2000 cycles. The steady-state, time-scale stability behavior indicates the excellent reversibility operation during cycling and the loss absence from parasitic processes, such as the electrolyte decomposition. Indeed, these full-scale LIB models attained approximately 100% of its Coulombic efficiency even at a considerable number of cycles.

Together, our proposed full-scale WG@C//AR@C LIB with open cave-in-hollow nests, spherule-rich interstitial core cavity-like sinks and circularly-shaped topography provides high value of specific energy density around 131.6 Wh kg^{-1}. This value achieves the mandatory requirements of energy density limit and driving range for long-term EVs. The spherule-generating
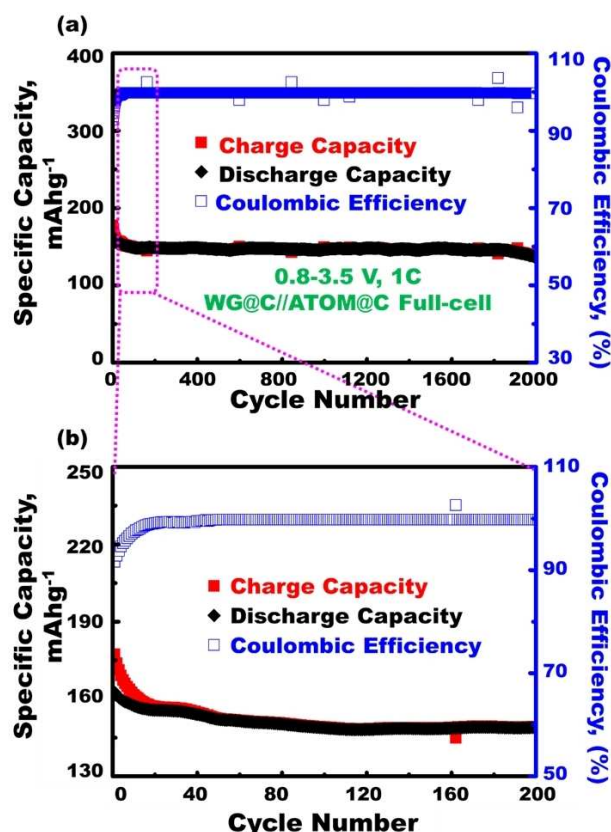
Figure 9. (a) Long-term cycling performance (stability) and Coulombic efficiency for heterogeneous spherical-built-in WG@C//AR@C full-scale LIB-model, at rate of 1 C up to 2000 cycles, voltage range 0.8–3.5 V at room temperature. (b) Enlarged cycling performance (stability) and Coulombic efficiency heterogeneous spherical-geodes built-in WG@C//AR@C full-scale LIB-model at rate of 1 C up to 200 cycles.

nests significantly guided the full-scale G@C//AR@C LIB design sets to (i) motivate the dynamic mobility of electron-ion motion systems directly, (ii) create a vehicle/truck storage loading, and (iii) retain the force-driven modulation of the high energy density full-scale LIB design during long-term charge/discharge processes (Scheme 2). Our finding shows real-space of evidence of the effect of structurally folded curvature surface models of vehicle folds on fabrication of anode/cathode LIB designs. It is technically first report of design full-scale G-cathode//AR-anode LIBs similar to those of vehicle/truck storages, such as high energy density, long periods of charge/discharge cycles, high Coulombic efficiency and discharge specific capacity, respectively.

3. Conclusions

We report first evidence of the effect of structurally folded curvature surface models of vehicle folds with a bundle of convex/concave spheroid-capped gradients on the creation of anode/cathode LIB designs similar to those of vehicle/truck storages. In this regard, structural vehicle folds were designated with a diverse of 3D surface vacancies included cave-in-hollow

nests, shell-walled/fenced edges, and convex/concave spheroid-capped gradients. These 3D surface curvature LFPO G-cathode/AR-anode electrodes were used as the force-driven modulation of high energy density of LIB-EV. A full-scale LFPO@C//AR@C built-in LIB vehicle/truck storage is formulated to motivate the dynamic mobility of electron-ion motion systems and create vehicle/truck storage loading during long-term charge/discharge cycling and stability electrochemical performance. Well-defined geometric LIB electrode features can be built by using variable spheroid curvature folds with WG-, EG-, and UG-cathode geode dominants and AR-anode, thus creating significant surface curvature function changes in sustainable nanodynamic electron-ion motion systems within multiple charge/discharge processes. These findings indicate that the WG@C half-cell cathode LIB design showed the most significant advancement in electrochemical performance among all the built-in LIB designs with (i) a capacity of 168.3 mAh g^{-1} at 0.1 C rate and 132.7 mAh g^{-1} at 20 C, (ii) durability after 2000 charge/discharge cycles without clear retrogradation, and (iii) high energy density. In the design of a powerful operation, the built-in full-scale WG@C-cathode// AR@C-anode LIB model as vehicle/truck storages leads to massive gate-in-transport of electron/Li$^+$ ion for long periods of charge/discharge cycles and outstanding discharge capacities.

The integration of potential built-in full-scale LIBs formulated with WG@C (cathode)//AR@C (anode) generated long-term stability in the cycling performance, rapid Li$^+$ ion conductor, 3D Li$^+$ ion diffusion paths, and facile lithiation and delithiation processes with excellent discharge capacity retention (approximately 85%) and average Coulombic efficiency at 99.6% after 2000 cycles at 1 C rate, a voltage range of 0.8–3.5 V, and excellent value of specific energy density at around ≈131.6 Wh kg^{-1}, respectively. The proposed LIB vehicle/truck storages contends the critical energy storage requirement and meets the industrial and commercial demands of the EV driving range in terms of high capacity, high energy and power density, safety characteristics, and cycling durability.

Experimental Section

Synthesis of Structurally-Folded Curvature Surface Models of LFPO Geodes (G-Cathode)

Lithium anion-assisted formulation (i.e. addition of LiCl, LiF, and LiNO$_3$ to composition domains) was a key broadening control of structurally-shaped spheroids along whole-, eroded- and un-opened geode dominants (WG-, EG-, and UG-cathode, respectively) as positive cathode electrodes. The synthesis of cave-in-hollow geode structures was dependent of the addition of variable Li-anions to the composition fabrication domains. The elemental molar ratios of Li:Fe:P in composition dominates of iron (III) acetylacetonate, phosphoric acid, and Li-anions were equivalent to 3:1:1. Significantly, the addition of LiCl, LiF, and LiNO$_3$ to composition domains of iron (III) acetylacetonate/phosphoric acid would enable to significant changes in 3D-surface curvature vehicle-like geode folds, offering a bundle of convex/concave spheroid-capped WG-, EG-, and UG-gradients. In typical synthesis,

each sample solution (i.e., phosphoric acid or iron (III) acetylacetonate) was firstly prepared by dissolving in mixture of 5 ml MilliQ-water, 2.55 ml ethanol, and 3000 μl ethylene glycol and then stirred separately for 1 hour. After 1 h stirring of two sample solution, the phosphoric acid solution added drop wise (0.5 ml/min) to the iron (III) acetylacetonate solution under continuous stirring for another 1 h. Finally, a solution of Li-chloride dissolved in 10 ml MilliQ-water, 5 ml ethanol, and 6000 μl ethylene glycol was stirred for 1 h at 30 °C. The Li-anion solution was dropwise added to the iron (III) acetylacetonate/phosphoric acid mixture with rate (0.5 ml/min), where the total molar ratios of Li:Fe:P are equivalent to 3:1:1 in the mixture. The final geode mixture was treated under vigorous magnetic stirring for other 6 h, pH solutions of 7. The final mixtures of WG were transferred into a 100 mL of Teflon-lined stainless-steel autoclaves. The autoclaves were maintained at 170 °C for 12 h and cooled to room temperature. The resulting solid products of WG were centrifuged, washed three times with Milli-Q-water and absolute ethanol and then dried overnight at 60 °C under vacuum. The final powder product was calcined at 600 °C for 6 hours leading to form 3D reconstructed geode structures. Using the same procedures, pH solutions of 7, and molar ratios of the Li:Fe:P (i.e., 3:1:1); however different Li-sources were used as follows lithium chloride, fluoride and nitrate for fabrication of WG, EG and UG spheroids, respectively (see Supporting Information S2).

Synthesis of 3D-Surface Curvature TO Agate Rosettes (AR-Anode)

In typical synthesis, a 159.93 mg titanium oxysulfate was dissolved in mixture of 20 ml milliQ-water and 20 ml ethanol to form a homogenous solution. A 3 ml H_2O_2 solution was added drop-wise at rate 0.5 ml/min under vigorous magnetic stirring for 2 h. The final mixture with pH = 9.2 was transferred into a 100 mL of Teflon-lined stainless-steel autoclaves. The autoclaves were maintained at 170 °C for 12 h and cooled to room temperature. The resulting solid products were centrifuged, washed three times with Milli-Q-water and absolute ethanol and then dried overnight at 60 °C under vacuum. The final powder product was calcined at 600 °C for 3 hours to form anatase-TO agate rosettes (AR-anode) with concave cave-in-hollow and convex orientation with mushroom-like surfaces (see Supporting Information S3).

Control Design of Heterogeneous G@C-Cathode and AR@C-Anode Composites

The carbon-capped spheroid gradients of 3D-surface curvature geodes (G-cathode)/agate rosettes (AR-anode) can be fabricated by using microwave-assisted method, in which the carbon source (i.e., 5w/w% glucose) was dispersed into G- and AR-powder materials and irradiated at 80 °C. In typical synthesis, the 5 w/w% glucose/G- and AR-powder mixture was sonicated in ethanol for 15 minutes. The mixtures were transferred to autoclaves and constantly stirred for another 30 minutes in microwave irradiation at 80 °C, and for 0.5 h. The color of the mixtures gradually turned to black. The precipitates were collected using centrifuge machine, washed by milli-Q water and ethanol. Finally, both precipitates were dried overnight at 55 °C in an electric oven. The resulting samples were milled separately in mortar and then calcined in Ar atmosphere at 350 °C for 0.5 h, and then set at 600 °C for 2 h with heating rate 5 °C/min. Under this simple condition, the carbon-shell layers were structurally-shaped spherule-rich interstitial core cavity-like sinks and circularly-shaped topography of (i) whole-, eroded- and un-opened geode dominants (WG@C-, EG@C-, and UG@C-cathode, respectively) as positive cathode electrodes and (ii) TO agate

rosette AR@C as negative anode electrodes, respectively (see Supporting Information S3–S9).

Fabrication of CR2032 Coin Cells with Half- and Full-Scale G@C-Cathode//AR@C-Anode LIBs

Structurally-folded curvature surface anode/cathode models were used in fabrication of CR2032 coin cells with half- and full-scale G@C-cathode//AR@C-anode LIB vehicle/truck storages. To show the key role of (i) cave-in-hollow, (ii) shell-walled/fenced edges, (iii) degree of 3D-surface curvature, and (iv) convex/concave spheroid-capped gradients in design of LIBs, the powerful AR@C (anode) and WG@C, EG@C and UG@C (cathodes) built-up electrode sets. Designs of half-cell anode or cathode and full-cell of cathode//anode building-blocks were configured similar to those of vehicle/truck storages. Structural vehicle folds were designated with WG@C//AR@C cathode//anode full-scale LIB-model under optimized mass loading (see Supporting Information S1&S12). The optimization of full cell (balancing) (N/P) ratio, full-scale cathode//anode stacked layers pouch LIB-model, mass loading, areal capacity and volumetric energy density was controlled to built-in LIB vehicle/truck storages. Within a CR2032 coin cell design of LIB-half cell cathode or anode, circular reference and counter electrodes with diameters of 16 mm of Li foil were used. In addition, the working electrodes and a 20 mm of separator were punched to control the electrochemical performances of the spherule-rich half-scale AR@C LIB-anode and spheroid-geode WG@C, EG@C and UG@C LIB-cathode models. Crimper machine for the CR20XX series coin cells utilized to press our 2032-coin cells inside the glove box under Ar. In addition, we designated WG@C//AR@C as anode//cathode full-cell LIBs for electrochemical measurements of full-system level design of stacked layers pouch LIB-model (Figure S1). In details, the configurations of half-and -built-in full-scale LIB-modulated vehicle/truck storages in CR2032 coin cells were controlled under specific protocols, as reported in the patterning steps at Supporting Information S1.

Conflict of Interest

The authors declare no conflict of interest.

Keywords: lithium-ion battery · 3D surface curvature geode · vehicle folds · high energy density · electrode design

[1] a) S. Li, Q. Wu, D. Zhang, Z. Liu, Y. He, Z. L. Wang, C. Sun, *Nano Energy* **2019**, *56*, 555–562; b) Y. Zhong, X. Xu, W. Wang, Z. Shao, *Batteries & Supercaps* **2019**, *2*, 272–289; c) X. Zhang, P. Dong, M.-K. Song, *Batteries & Supercaps* **2019**, *2*, 591–626.

[2] a) S. Nishimura, G. Kobayashi, K. Ohoyama, R. Kanno, M. Yashima, A. Yamada, *Nat. Mater.* **2008**, *7*, 707–711; b) W. Li, R. Fang, Y. Xia, W. Zhang, X. Wang, X. Xia, J. Tu, *Batteries & Supercaps* **2019**, *2*, 9–36.

[3] a) H. Gomaa, M. A. Shenashen, H. Yamaguchi, A. S. Alamoudi, S. A. El-Safty, *Green Chem.* **2018**, *20*, 1841–1857; b) H. Gomaa, S. A. El-Safty, M. A. Shenashen, S. Kawada, H. Yamaguchi, M. Abdelmottaleb, M. F. Cheira, *ACS Sustainable Chem. Eng.* **2018**, *6*, 13813–13825; c) S. A. El-Safty, Md. R. Awual, M. A. Shenashen, A. Shahat, *Sens. Actuators B* **2013**, *176*, 1015–1025.

[4] a) W. Zhang, Y. Fu, W. Liu, L. Lim, X. Wang, A. Yu, *Nano Energy* **2019**, *57*, 48–56; b) C. Liu, Z. G. Neale, G. Cao, *Mater. Today* **2016**, *19*, 109–123.

[5] a) A. K. Padhi, K. S. Nanjundaswamy, J. B. Goodenough, *J. Electrochem. Soc.* **1997**, *144*, 1188–1194; b) W. Zhang, Y. Fu, W. Liu, L. Lim, X. Wang, A. Yu, *Nano Energy* **2019**, *57*, 48–56.

[6] a) M. Y. Emran, N. Akhtar, M. Mekawy, M. A. Shenashen, I. M. El-Sewify, A. Faheem, S. A. El-Safty, *Biosens. Bioelectron.* **2018**, *100*, 122–131; b) M. Y. Emran, S. A. El-Safty, M. A. Shenashen, T. Minowa, *Sens. Actuators B* **2019**, *284*, 456–467; c) M. Y. Emran, M. A. Shenashen, H. Morita, S. A. El-Safty, *Adv. Healthcare Mater.* **2018**, *7*, 1701459; d) M. Y. Emran, M. A. Shenashen, A. A. Abdelwahab, H. Khalifa, M. Mekawy, N. Akhtar, M. Abdelmottaleb, S. A. El-Safty, *J. Appl. Electrochem.* **2018**, *48*, 529–542.

[7] a) K. Kanamura, S. Koizumi, K. Dokko, *J. Mater. Sci.* **2008**, *43*, 2138–2142; b) G. Meligrana, C. Gerbaldi, A. Tuel, S. Bodoardo, N. Penazzi, *J. Power Sources* **2006**, *160*, 516–522.

[8] a) M. Zhang, N. Garcia-Araez, A. L. Hector, *J. Mater. Chem. A* **2018**, *6*, 14483–14517; b) A. V. Murugan, T. Muraliganth, A. Manthiram, *Chem. Mater.* **2009**, *21*, 5004–5006; c) A. V. Murugan, T. Muraliganth, A. Manthiram, *Chem. Mater.* **2009**, *21*, 5004–5006; d) Y. Jin, X. Tang, Y. Wang, W. Dang, J. Huang, X. Fang, *CrystEngComm* **2018**, *20*, 6695–6703.

[9] a) Y. Jin, X. Tang, Y. Wang, W. Dang, J. Huang, X. Fang, *CrystEngComm* **2018**, *20*, 6695–6703; b) Y. Jiang, R. Tian, H. Liu, J. Chen, X. Tan, L. Zhang, G. Liu, H. Wang, L. Sun, W. Chu, *Nano Res.* **2015**, *8*, 3803–3814.

[10] L. Guo, Y. Zhang, J. Wang, L. Ma, S. Ma, Y. Zhang, E. Wang, Y. Bi, D. Wang, W. C. McKee, Y. Xu, J. Chen, Q. Zhang, C. Nan, L. Gu, P. G. Bruce, Z. Peng, *Nat. Commun.* **2015**, *6*, 7898.

[11] a) A. Vadivel Murugan, T. Muraliganth, A. Manthiram, *J. Electrochem. Soc.* **2009**, *156*, A79–A83; b) K. Zaghib, A. Mauger, F. Gendron, C. M. Julien, *Chem. Mater.* **2008**, *20*, 462–469.

[12] a) J. K. Kim, J. W. Choi, G. Cheruvally, J. U. Kim, J. H. Ahn, G. B. Cho, K. W. Kim, H. J. Ahn, *Mater. Lett.* **2007**, *61*, 3822–3825; b) C. Z. Lu, G. T. K. Fey, H. M. Kao, *J. Power Sources* **2009**, *189*, 155–162; c) K. Wang, R. Cai, T. Yuan, X. Yu, R. Ran, Z. Shao, *Electrochim. Acta* **2009**, *54*, 2861; d) G. T. K. Fey, T. L. Lu, *J. Power Sources* **2008**, *178*, 807–814.

[13] a) H. Liu, H. Yang, J. Li, *Electrochim. Acta* **2010**, *55*, 1626–1629; b) J. Liu, J. Wang, X. Yan, X. Zhang, G. Yang, A. F. Jalbout, R. Wang, *Electrochim. Acta* **2009**, *54*, 5656–5659.

[14] a) M. Wagemaker, B. L. Ellis, D. Lützenkirchen-Hecht, F. M. Mulder, L. F. Nazar, *Chem. Mater.* **2008**, *20*, 6313–6315; b) G. Qin, S. Xue, Q. Ma, C. Wang, *CrystEngComm* **2014**, *16*, 260–269.

[15] a) Z. Tian, Z. Zhou, S. Liu, F. Ye, S. Yao, *Solid State Ionics*, **2015**, *278*, 186–191; b) X. Qin, J. Wang, J. Xie, F. Li, L. Wen, X. Wang, *Phys. Chem. Chem. Phys.* **2012**, *14*, 2669–2677; c) M. K. Devaraju, I. Honma, *Adv. Energy Mater.* **2012**, *2*, 284–297.

[16] a) A. Singhal, G. Skandan, G. Amatucci, F. Badway, N. Ye, A. Manthiram, H. Ye, J. J. Xu, *J. Power Sources* **2004**, *129*, 38–44; b) K. S. Park, J. T. Son, H. T. Chung, S. J. Kim, C. H. Lee, K. T. Kang, H. G. Kim, *Solid State Commun.* **2004**, *129*, 311–314.

[17] a) M. Takahashi, S. Tobishima, K. Takei, Y. Sakurai, *J. Power Sources* **2001**, *97–98*, 508–511; b) T. H. Cho, H. T. Chung, *J. Power Sources* **2004**, *133*, 272–276.

[18] S. Lee, Y. Cho, H. K. Song, K. T. Lee, J. Cho, *Angew. Chem. Int. Ed.* **2012**, *51*, 8748–8752.

[19] a) D. Hassen, M. A. Shenashen, A. R. El-Safty, A. Elmarakbi, S. A. EL-Safty, *Sci. Rep.* **2018**, *8*, 3740; b) M. A. Shenashen, D. Hassen, S. A. El-Safty, H. Isago, A. Elmarakbi, H. Yamaguchi, *Chem. Eng. J.* **2017**, *313*, 83–98; c) D. K. Hassen, M. M. Selim, S. A. El-Safty, K. A. Khalil, G. Abu el-Maged, M. Dewidar, *Nano-Structures & Nano-Objects* **2017**, *9*, 31–39; d) D. Hassen, S. A. El-Safty, K. Tsuchiya, A. Chatterjee, A. Elmarakbi, M. A. Shenashen, M Sakai, *Sci. Rep.* **2016**, *6*, 24330; e) D. Hassen, M. A. Shenashen, S. A. El-Safty, M. M. Selim, H Isago, A Elmarakbi, A El-Safty, H Yamaguchi, *J. Power Sources* **2016**, *330*, 292–303; f) D. Hassen, S. A. El-Safty, N. Akhtar, A. Chatterjee, A. Elmarakbi, *Adv. Mater. Interfaces* **2016**, *3*, 1600743.

[20] a) M. Khairy, S. A. El-Safty, *Chem. Commun.* **2014**, *50*, 1356; b) M. Khairy, S. A. El-Safty, *J. Energy Chem.* **2015**, *24*, 31–38; c) M. Khairy, S. A. El-Safty, *Sens. Actuators B* **2014**, *193*, 644–652; d) M. Khairy, S. A. El-Safty, *RSC Adv.* **2013**, *3*, 23801–23809.

[21] a) M. Broussely, P. Biensan, B. Simon, *Electrochim. Acta* **1999**, *45*, 3–22; b) Y. Nishi, *J. Power Sources* **2001**, *100*, 101–106; c) M. Aldissi, *J. Power Sources* **2001**, *94*, 219–224.

[22] a) J. Wen, Y. Yu, C. Chen, *Mater. Express* **2012**, *2*, 197–212; b) C. Uhlmann, J. Illig, M. Ender, R. Schuster, E. Ivers-Tiffée, *J. Power Sources* **2015**, *279*, 428–438; c) T. M. Bandhauer, S. Garimella, T. F. Fuller, *J. Electrochem. Soc.* **2011**, *158*, R1–R25.

[23] a) L. Xu, C. Kim, A. K. Shukla, A. Dong, T. M. Mattox, D. J. Milliron, J. Cabana, *Nano Lett.* **2013**, *13*, 1800–1805; b) F. F. Cao, J. W. Deng, S. Xin,

H. X. Ji, O. G. Schmidt, L. J. Wan, Y. G. Guo, *Adv. Mater.* **2011**, *23*, 4415–4420; c) X. Fan, H. Zhang, N. Du, P. Wu, X. Xu, Y. Li, D. Yang, *Nanoscale* **2012**, *4*, 5343–5347; d) L. Ji, Z. Lin, M. Alcoutlabi, X. Zhang, *Energy Environ. Sci.* **2011**, *4*, 2682–2699.

[24] Y. S. Hu, L. Kienle, Y. G. Guo, J. Maier, *Adv. Mater.* **2006**, *18*, 1421–1426.

[25] a) S. J. Bao, Q. L. Bao, C. M. Li, Z.-L. Dong, *Electrochem. Commun.* **2007**, *9*, 1233; b) B. Breitung, A. Schneider, V. S. K. Chakravadhanula, C. Suchomski, J. Janek, H. Sommer, T. Brezesinski, *Batteries& Supercaps* **2018**, *1*, 27–32.

[26] a) J. Wang, Y. Bai, M. Wu, J. Yin, W. F. Zhang, *J. Power Sources* **2009**, *191*, 614–618; b) Y. Wang, M. Wu, W. F. Zhang, *Electrochim. Acta* **2008**, *53*, 7863–7868.

[27] a) V. Aravindan, Y. S. Lee, R. Yazami, S. Madhavi, *Mater. Today* **2015**, *18*, 345–351; b) G. F. Ortiz, I. Hanzu, T. Djenizian, P. Lavela, J. L. Tirado, P. Knauth, *Chem. Mater.* **2009**, *21*, 63–67; c) X. Zhang, V. Aravindan, P. S. Kumar, H. Liu, J. Sundaramurthy, S. Ramakrishna, S. Madhavi, *Nanoscale* **2013**, *5*, 5973–5980.

[28] a) W. Warkocki, S. A. El-Safty, M. A. Shenashen, E. Elshehy, H. Yamaguchi, N. Akhtar, *J. Mater. Chem. A.* **2015**, *3*, 17578–17589; b) H. Gomaa, M. A. Shenashen, H. Yamaguchi, A. S. Alamoudi, M. Abdelmottaleb, M. F. Cheira, T. A. S. El-Naser, S. A. El-Safty, *J. Cleaner Prod.* **2018**, *182*, 910–925; c) H. G. Gomaa, H. Khalifa, M. Selim, M. A. Shenashen, S. Kawada, A. S. Alamoudi, A. Azzam, A. Alhamid, S. A. El-Safty, *ACS Sustainable Chem. Eng.* **2017**, *5*, 10826–10839; d) A. Aboelmagd, S. A. El-Safty, M. A. Shenashen, E. A. Elshehy, M. Khairy, M. Sakai, H. Yamaguchi, *Chem. Asian J.* **2015**, *10*, 2467–2478.

[29] a) C. Sun, S. Rajasekhara, J. B. Goodenough, F. Zhou, *J. Am. Chem. Soc.* **2011**, *133*, 2132–2135; b) J. Su, X. L. Wu, C. P. Yang, J. S. Lee, J. Kim, Y. G. Guo, *J. Phys. Chem. C* **2012**, *116*, 5019–5024.

[30] a) X. Huang, S. Yan, H. Zhao, L. Zhang, R. Guo, C. Chang, X. Kong, H. Han, *Mater. Charact.* **2010**, *61*, 720–725; b) B. Ellis, W. H. Kan, W. R. M. Makahnouk, L. F. Nazar, *J. Mater. Chem.* **2007**, *17*, 3248–3254.

[31] D. Chen, W. Wei, R. Wang, X. F. Lang, Y. Tian, L. Guo, *Dalton Trans.* **2012**, *41*, 8822–8828.

[32] a) J. C. Zheng, X. H. Li, Z. X. Wang, H. J. Guo, S. Y. Zhou , *J. Power Sources* **2008**, *184*, 574; b) S. A. El-Safty, M. A. Shenashen, M. Ismael, M. Khairy, *Adv. Funct. Mater.* **2012**, *22*, 3013–3021; c) M. Y. Emran, M. A. Shenashen, M. Mekawy, A. M. Azzam, N. Akhtar, H. Gomaa, M. M. Selim, A. Faheem, S. A. El-Safty, *Sens. Actuators B* **2018**, *259*, 114–124.

[33] a) W. Zhang, X. Zhou, X. Tao, H. Huang, Y. Gan, C. Wang, *Electrochim. Acta* **2010**, *55*, 2592; b) N. Akhtar, M. Y. Emran, M. A. Shenashen, H. Khalifa, T. Osaka, A. Faheem, T. Homma, H. Kawarada, S. A. El-Safty, *J. Mater. Chem. B* **2017**, *5*, 7985–7996.

[34] a) M. Y. Emran, M. A. Shenashen, H. Morita, S. A. El-Safty, *Biosens. Bioelectron.* **2018**, *190*, 237–245; b) M. Y. Emran, M. A. Shenashen, A. A. Abdelwahab, M. Abdelmottaleb, M. Khairy, S. A. El-Safty, *Electrocatalysis* **2018**, *9*, 514–525; c) M. Y. Emran, M. A. Shenashen, A. A. Abdelwahab, M. Abdelmottaleb, S. A. El-Safty, *New J. Chem.* **2018**, *42*, 5037–5044.

[35] a) N. Akhtar, S. A. El-Safty, M. E. Abdelsalam, M. Shenashen, H. Kawarada, *Biosens. Bioelectron.* **2016**, *77*, 656–665; b) M. Y. Emran, H. Khalifa, H. Gomaa, M. A. Shenashen, N. Akhtar, M. Mekawy, A. Faheem, S. A. El-Safty, *Microchim. Acta* **2017**, *184*, 4553–4562; c) N. Akhtar, S. A. El-Safty, M. E. Abdelsalam, H. Kawarada, *Adv. Healthcare Mater.* **2015**, *4*, 2110–2119; d) N. Akhtar, S. A. El-Safty, M. E. Abdelsalam, H. Kawarada, *Nano-Structures & Nano-Objects* **2015**, *2*, 35–44.

[36] a) J. Hassoun, F. Bonaccorso, M. Agostini, M. Angelucci, M. G. Betti, R. Cingolani, M. Gemmi, C. Mariani, S. Panero, V. Pellegrini, B. Scrosati, *Nano Lett.* **2014**, *14*, 4901–4906; b) N. Akhtar, S. A. El-Safty, M. Khairy, W. Ahmed, *Chemosensors* **2014**, *2*, 235–250; c) N. Akhtar, S. A. El-Safty, M. Khairy, W. A. El-Said, *Sens. Actuators B* **2015**, *207*, 158–166.

[37] D. Choi, D. Wanga, V. V. Viswanathan, I.-T. Bae, W. Wang, Z. Nie, J.-G. Zhang, G. L. Graff, J. Liu, Z. Yang, T. Duong, *Electrochem. Commun.* **2010**, *12*, 378–381.